# การออกแบบขั้วสัมผัสผิวหน้าที่เหมาะที่สุดของเซลล์สุริยะ

นายชาญวิทย์ เรืองเฉลิมวงศ์



วิทยานิพนธ์นี้เป็นส่วนหนึ่งของการศึกษาตามหลักสูตรปริญญาวิทยาศาสตรมหาบัณฑิต
สาขาวิชาฟิสิกส์ ภาควิชาฟิสิกส์
คณะวิทยาศาสตร์ จุฬาลงกรณ์มหาวิทยาลัย
ปีการศึกษา 2547

ISBN 974-17-7137-1

# OPTIMAL DESIGN OF SOLAR CELL FRONT-CONTACT GRID

Mr. Charnwit Ruangchalermwong

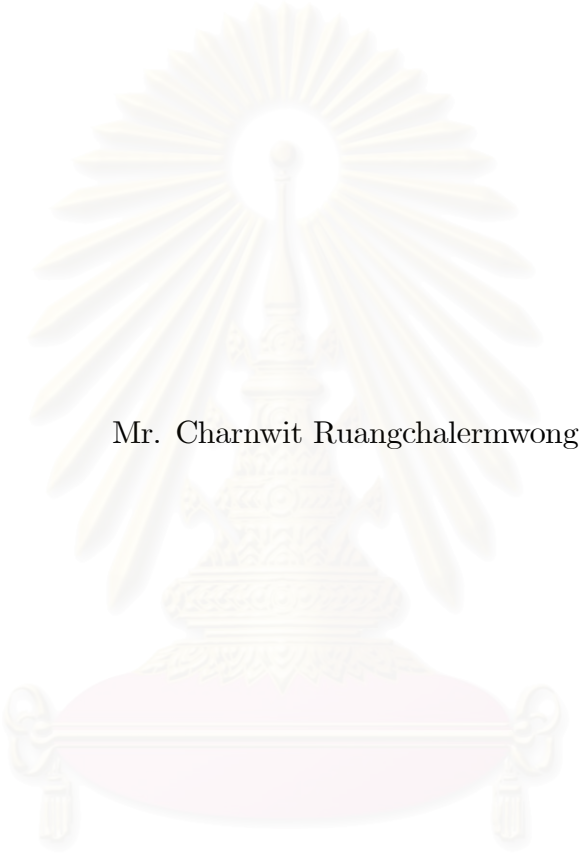



A Thesis Submitted in Partial Fulfillment of the Requirements
for the Degree of Master of Science in Physics
Department of Physics
Faculty of Science
Chulalongkorn University
Academic Year 2004

ISBN 974-17-7137-1

| | |
|---|---|
| Thesis Title | Optimal Design of Solar Cell Front-Contact Grid |
| By | Mr. Charnwit Ruangchalermwong |
| Field of Study | Physics |
| Thesis Advisor | Assistant Professor Kajornyod Yoodee, Ph.D. |
| Thesis Co-advisor | Sojiphong Chatraphorn, Ph.D. |

---

Accepted by the Faculty of Science, Chulalongkorn University in Partial Fulfillment of the Requirements for the Master's Degree

..... Dean of the Faculty of Science
(Professor Piamsak Menasveta, Ph.D.)

THESIS COMMITTEE

..... Chairman
(Associate Professor Wichit Sritrakool, Ph.D.)

..... Thesis Advisor
(Assistant Professor Kajornyod Yoodee, Ph.D.)

..... Thesis Co-advisor
(Sojiphong Chatraphorn, Ph.D.)

..... Member
(Chatchai Srinitiwarawong, Ph.D.)

..... Member
(Sathon Vijarnwannaluk, Ph.D.)

ชาญวิทย์ เรืองเฉลิมวงศ์ : การออกแบบขั้วสัมผัสที่ผิวหน้าที่เหมาะสมที่สุดของเซลล์สุริยะ. (OPTIMAL DESIGN OF SOLAR CELL FRONT-CONTACT GRID) อ. ที่ปรึกษา : ผศ.ดร.ขจรยศ อยู่ดี, อ.ที่ปรึกษาร่วม : ดร.โศจิพงศ์ ฉัตราภรณ์, 70 หน้า. ISBN 974-17-7137-1.

งานวิจัยนี้ได้ทำการออกแบบหาลวดลายของขั้วสัมผัสโลหะที่ผิวหน้าของเซลล์สุริยะ เพื่อให้ได้เซลล์ที่มีประสิทธิภาพสูง การคำนวณได้อาศัยรูปแบบการต่อกันของเซลล์ย่อยและกฎการคำนวณกระแสของ Kirchhoff เพื่อตั้งระบบสมการ นอกจากนี้ยังได้ใช้กระบวนการเชิงตัวเลขเพื่อแก้หาคำตอบสำหรับกระแสไฟฟ้าที่ผลิตได้ในแต่ละค่าความต่างศักย์ไฟฟ้าที่กำหนด เซลล์สุริยะที่ศึกษาในงานวิจัยนี้ได้มุ่งเน้นที่เซลล์สุริยะชนิดฟิล์มบางที่มีโครงสร้างแบบ Cu(In,Ga)$Se_2$/CdS/ZnO/ขั้วสัมผัสโลหะ ทั้งนี้พบว่ากระแสไฟฟ้าที่ผลิตจากแสงในโครงสร้างของเซลล์มีค่าน้อยกว่า 35 mA/$cm^2$ และไม่คงที่ กระบวนการเชิงตัวเลขได้ถูกนำมาใช้ในการหาลักษณะเฉพาะกระแส-ความต่างศักย์ไฟฟ้าของเซลล์สุริยะข้างต้นที่ได้สมมุติขั้วสัมผัสโลหะ เพื่อหาประสิทธิภาพของเซลล์ การออกแบบได้ประมาณความสัมพันธ์ระหว่างค่าความยาวการแพร่ และความกว้างของเซลล์เพื่อให้ได้เซลล์ที่มีประสิทธิภาพดีที่สุดซึ่งพบว่าความกว้างของเซลล์ที่เหมาะสมมีค่าเพิ่มขึ้นตามค่าของความยาวการแพร่ที่มากขึ้น ขณะที่ความกว้างของเซลล์ที่เหมาะสมไม่เกิดขึ้นภายใต้ค่าความยาวการแพร่ที่มีค่าต่ำ นอกจากนี้การออกแบบยังได้ทำการหาค่าตัวแปรของขั้วสัมผัสแบบรูปส้อมที่มีแขนขนานกันสองข้างได้แก่ค่าระยะห่างระหว่างแขน และค่าความกว้างของแขนแต่ละข้าง โดยค่าระยะห่างระหว่างแขนของขั้วสัมผัสที่เหมาะสมมีค่าเพิ่มขึ้นเมื่อค่าความต้านทานแบบแผ่นมีค่ามากขึ้น ผลการวิเคราะห์ไม่แสดงให้เห็นค่าความกว้างของแขนที่ให้ค่าประสิทธิภาพดีที่สุดสำหรับทุกค่าความต้านทานแบบแผ่นที่กำหนด ประสิทธิภาพของเซลล์ที่ได้มีค่าขึ้นกับค่าความต้านทานแบบแผ่นที่ใช้ด้วย



ภาควิชา.....ฟิสิกส์..... ลายมือชื่อนิสิต.....

สาขาวิชา.....ฟิสิกส์..... ลายมือชื่ออาจารย์ที่ปรึกษา.....

ปีการศึกษา.....2547..... ลายมือชื่ออาจารย์ที่ปรึกษาร่วม.....

# # 447 22493 23 : MAJOR PHYSICS
KEY WORDS: OPTIMIZATION / DISTRIBUTED NETWORK MODEL / GRID / SOLAR CELL

CHARNWIT RUANGCHALERMWONG : OPTIMAL DESIGN OF SOLAR CELL FRONT-CONTACT GRID. THESIS ADVISOR: ASST. PROF. KAJORNYOD YOODEE, Ph.D., THESIS CO-ADVISOR: SOJIPHONG CHATRAPHORN, Ph.D., 70 pp. ISBN 974-17-7137-1.

In order to obtain high efficiency solar cells, the front contact metal grid must be optimized to attain the appropriate grid pattern. An optimization procedure based on a distributed network model and Kirchoff's current law forming a system of equations was carried out and solved for a solution of an output current for each boundary voltage. In this work, we focused on a multilayer thin film solar cell based on the structure Cu(In,Ga)$Se_2$/CdS/ZnO/metal-grid. The photo-generated current, which was found to be less than 35 mA/$cm^2$, varied as a function of the boundary voltage. A numerical technique was used to find the current-voltage characteristics and the efficiency for an assumed grid pattern. The optimization estimated the relationship between diffusion length and the width of the cell for best cell efficiency. The longer the diffusion length was, the larger the optimal width of the cell could be obtained. However, the optimum was not occured in short diffusion length. Furthermore, the optimization for fork-shaped grid patterns with two parallel arms was performed to achieve grid parameters, e.g. the spacing between the two arms and the width of each arm. As sheet resistance increased, the optimal value of the spacing between the two arms increased but that of the width of each arm did not happen. However, the efficiency depends strongly on the sheet resistance.

Department ..... Physics ..... Student's signature .....
Field of study .... Physics ..... Advisor's signature .....
Academic year ... 2004 ..... Co-advisor's signature .....

# Acknowledgements

I would like to express my sincere gratitude to my thesis advisors, Assistant Professor Dr. Kajornyod Yoodee and Dr. Sojiphong Chatraphorn for their valuable suggestions, helps and discussion. I am also particularly grateful to Dr. Chanwit Chityuttakan for analysing the problem during the period of this study, and suggesting the way to handle it.

I wish to express my special thanks to the thesis committee, Associate Professor Dr. Wichit Sritakool, Dr. Chatchai Srinitiwarawong and Dr. Sathon Vijarnwannaluk for their reading and criticizing.

I wish to express my great gratitude to my parents who always believe in and support me in every way that they can.

Many thanks to my friends and the people associated with me for their encouragement.

Finally, I would like to acknowledge a financial support from the Development and Promotion of Science and Technology Talent Project of Thailand (DPST), the Department of Physics and the Graduate School of Chulalongkorn University.

# Table of Contents

**page**

# List of Figures

**page**

**page**

**page**

**page**

# List of Tables

**page**

# CHAPTER 1

# Introduction

Solar cells are photovoltaic devices that convert solar energy directly into electricity. They are considered as a major candidate for obtaining energy from the sun about 1,000 W/m$^2$ [1] because of their nearly permanent power at low operating cost with little or no emission of pollution and environmental friendly technology. When photon energies are above a certain threshold energy or band gap energy, the light will be absorbed in a semiconductor material and electron-hole pairs are created. If the electron-hole pairs are generated close enough to the pn-junction, the carriers can be separated by an internal electric field and contribute the generated current. By placing collector grids made of metal contacts on the top and bottom of a cell, we can draw that current off externally.

The high efficiency solar cell was first developed in 1954 [2]. It has been developed repeatedly for a long time until it gains more attention in thin film solar cells. Copper-Indium-Gallium-Diselenide (CIGS) thin film solar cells have achieved the highest efficiency of all thin film solar cells [3]. Its efficiency is approximately 18% for a laboratory scale [4]. According to its high efficiency, the CIGS solar cell attracts researchers to develop and take its advantage in many other ways.

To obtain high efficiency CIGS-based solar cells, composition of each layer of the solar cell must be studied and developed in order to obtain suitable properties, such as a) adjusting window layer in order to increase conductivity and still have enough light transmission [5] or b) increasing area exposed to light that enhances the current in an absorber layer [6]. Moreover, one important part in the solar cell is grids. Generally, aluminum metal is used as the grid material in order to bring

current out of the cell to an external load. It becomes much more useful if there is a concentrator system such as lens and mirror [7], therefore rising an amount of the photocurrent. There are power-loss mechanisms, such as ohmic loss and optical loss, occuring in the window layers of the solar cell with grid patterns. The optimal design of the grid pattern may be done by integrating these factors but in one dimension according to the grid length in order to determine the direction of the current perpendicular to the grid edge. Consequently, it is hard to evaluate quality of some grid shapes.

In our study, the grids are designed by using a distributed network model [8] for the cell with an assumed grid pattern on the surface using electrical parameters of each unit cell and Kirchhoff's current law. Our work will show the relationship between the diffusion length and the width of the solar cell. In addition, in order to obtain the highest efficiency of the solar cell using the fork-shaped grid pattern with two pararellel arms, two factors (shaded area of the covering grid and sheet resistance of the top layer) are used to optimize for grid parameters, the width of each arm and the spacing between the two arms. In addition, important parameters such as a fill factor, a short circuit current and an open circuit voltage must be evaluated simultaneously together with the cell efficiency.

## Objective

To optimize the design of the front-contact grid pattern for solar cells by considering the least electrical power loss.

## Research procedures

1. Calculate the photocurrent associated with CIGS-based solar cells under an illumination of air mass 1.5.

2. Make a set of equations for the solar cell with an assumed grid pattern by using a circuit model with previously calculated photocurrent and electrical parameters appearing in the model, especially sheet resistance of the top layer.

3. Solve the set of equations by using numerical methods to obtain the current-voltage characteristics of the cell.

4. Find the appropriate grid pattern according to the results for the best power efficiency.

## Thesis outline

This thesis is divided into three parts as follows. The first part consists of theoretical background of semiconductors, junctions and solar cells. These are discussed in Chapters 2 and 3. The second part in Chapter 4 describes the method, the circuit model and the calculation of the power efficiency for the solar cell with calculated photocurrent and assumed grid pattern. In the final part of this thesis, results (with discussions) and conclusions are presented in Chapters 5 and 6, respectively.

# CHAPTER 2

# Theoretical Background

In a simple way of saying, semiconductor is the material which can control the flow of the electrical current. It is widely used to make various electrical devices such as integrated circuits, lasers, photodetectors, electroluminescent diodes and solar cells. The aim of this chapter is to present the basics of semiconductor and semiconductor junctions.

## 2.1 Introduction

When atoms are brought closer together, the interaction between the electrostatic fields of these atoms splits the energy levels into bands of permitted energy. The permitted energy bands are separated by the energy band gap $E_g$ or forbidden band in which there is no allowed state. The band containing valence electrons is called the valence band and the outermost is called the conduction band. The top of the conduction band is known as the vacuum level. Electrons with greater energy than the binding energy can escape from the solid completely, as in thermionic emission.

The electrons in the conduction band or conduction electrons can move freely, thus carrying electric current. At higher temperatures, valence electrons with sufficient energy can be thermally excited leaving vacant sites. The vacant sites are equivalent to mobile positive charges, known as holes. The electrons from neighboring atom can fill the holes. This causes the motion of the holes. The electric current in the semiconductor is due to the motion of holes in the valence band and/or electrons in the conduction band.

## 2.2 Charge Carriers in Semiconductor [9,10]

For an intrinsic semiconductor, the number of conduction electrons in the conduction band are equal to the number of holes in the valence band:

$$n_i = p_{i,} \tag{2.1}$$

where $n_i$ and $p_i$ are the intrinsic electron number density and the intrinsic hole number density, respectively.

In order to quantify the number of charge carrier in semiconductor, we must know two pieces of important information:

1. The number of allowed states at energy $E$,
2. The probability of any given state being occupied.

There are no energy states in forbidden band gap but many energy states within permitted bands. The number of allowed states per unit volume and energy for the conduction band, $g_C(E)$, and the valence band, $g_V(E)$, are given by

$$g_C(E) = \frac{4\pi}{h^3}(2m_e^*)^{\frac{3}{2}}(E - E_C)^{\frac{1}{2}}, \tag{2.2}$$

and

$$g_V(E) = \frac{4\pi}{h^3}(2m_h^*)^{\frac{3}{2}}(E_V - E)^{\frac{1}{2}}, \tag{2.3}$$

where $m_e^*$ and $m_h^*$ are the effective mass of electrons and holes, respectively, and $E_C$ and $E_V$ are the bottom edge of the conduction band and the top edge of the valence band, respectively. For the intrinsic semiconductor, the Fermi energy $E_{Fi}$ is near the midgap. The probability of a state at an energy $E$ being occupied is given by the Fermi-Dirac distribution function, $f_{FD}(E)$:

$$f_{FD}(E) = \frac{1}{1 + \exp\left(\frac{E - E_{Fi}}{kT}\right)}. \tag{2.4}$$

If $E - E_{Fi}$ is much greater than kT, the Fermi-Dirac distribution can be reduced to the Boltzmann approximation:

$$f_{FD}(E) \cong \exp\left[-\left(\frac{E - E_{Fi}}{kT}\right)\right]. \tag{2.5}$$

The value for the electron number density in the thermal-equilibrium is

$$n_o = \int_{E_C}^{\infty} g_C(E) f_{FD}(E) dE. \tag{2.6}$$

Using the Boltzmann approximation and Eq.(2.2), the thermal equilibrium electron concentration in the conduction band is

$$n_o = \int_{E_C}^{\infty} \frac{4\pi}{h^3} (2m_e^*)^{\frac{3}{2}} (E - E_C)^{\frac{1}{2}} \exp\left[-\left(\frac{E - E_{Fi}}{kT}\right)\right] dE. \tag{2.7}$$

The result of the above integration is

$$n_o = \frac{2}{h^3} (2\pi m_e^* kT)^{\frac{3}{2}} \exp\left[-\left(\frac{E_C - E_{Fi}}{kT}\right)\right]. \tag{2.8}$$

The coefficient in front of the exponential term can be rewritten as the effective density of state function in the conduction band, $N_C$:

$$N_C = \frac{2}{h^3} (2\pi m_e^* kT)^{\frac{3}{2}}. \tag{2.9}$$

Then, the thermal equilibrium electron concentration in the conduction band is

$$n_o = N_C \exp\left[-\left(\frac{E_C - E_{Fi}}{kT}\right)\right]. \tag{2.10}$$

A similar analysis is performed for the thermal equilibrium concentration of holes in the valence band using $1 - f_{FD}(E)$, the probability of a state at an energy $E$ being empty in the valence band is

$$p_o = N_V \exp\left[\frac{E_V - E_{Fi}}{kT}\right], \tag{2.11}$$

where $N_V$ is the effective density of states in the valence band and is given by

$$N_V = \frac{2}{h^3} (2\pi m_h^* kT)^{\frac{3}{2}}. \tag{2.12}$$

If $n_o$ is greater than $p_o$, the semiconductor is called n-type. In an n-type semiconductor, electrons are referred as majority carriers and holes as minority carriers. In the contrary, p-type is the semiconductor in which $p_o$ is greater than $n_o$. Multiply $p_o$ with $n_o$, we obtain

$$n_o p_o = N_C N_V \exp\left[-\left(\frac{E_C - E_V}{kT}\right)\right] \tag{2.13}$$

or

$$n_o p_o = N_C N_V \exp\left[-\frac{E_g}{kT}\right]. \tag{2.14}$$

As $p_o$ and $n_o$ are equal in an intrinsic semiconductor, intrinsic electron concentration $n_i$ can be written from Eq.(2.14),

$$n_i = (N_C N_V)^{\frac{1}{2}} \exp\left(-\frac{E_g}{2kT}\right). \tag{2.15}$$

Equation (2.15) is similar to the Boltzmann approximation. $n_i$ is proportional to the number of electrons with an energy greater than $E_g$. The intrinsic Fermi energy can be found by equating $n_o$ and $p_o$ in Eqs.(2.10) and (2.11). Hence

$$E_{Fi} = \frac{1}{2}(E_C + E_V) + \frac{kT}{2}\ln\left(\frac{N_V}{N_C}\right) \tag{2.16}$$

$E_{Fi}$ is close to midgap when the effective densities of state $N_C$ and $N_V$ are equal. This means that the semiconductor is pure and perfect.

In the case of extrinsic semiconductor, we can express the position of the Fermi energy as a function of doping concentration and as a function of temperature. If all dopant atoms are ionized, we will approximate $n_o$ and $p_o$ as $n_o \approx N_D$ and $p_o \approx N_A$, where $N_D$ and $N_A$ are the concentration of donor atoms and acceptor atoms, respectively. The Fermi energy is given by

$$E_F = E_C - kT\ln\left(\frac{N_C}{N_D}\right), \tag{2.17}$$

in which the majority carriers are the donor atoms. For majority carrier being acceptor atom, the Fermi energy becomes

$$E_F = E_V + kT\ln\left(\frac{N_V}{N_A}\right). \tag{2.18}$$

Equation (2.14) is the product of $n_o$ and $p_o$ in term of fixed material properties and temperature, then

$$n_o p_o = CT^3 \exp\left[-\frac{E_g}{kT}\right], \tag{2.19}$$

where $C$ is a constant. The relation is also true for the semiconductor in thermal equilibrium, that is

$$n_o p_o = n_i^2. \tag{2.20}$$

This relation is more general than the case of pure semiconductors previously discussed.

## 2.3 Transport Property of Electrons and Holes [9]

The motion of electrons and holes in semiconductors is responsible for the electrical conduction due to an applied electric field. When the electric field is applied to the semiconductor, the electron will move with drift velocity $v_d$ under the influence of the electric field. The drift velocity of the electron is opposite to the direction of electric field since the electron has a negative charge. At small field, the drift velocity is proportional to the field, and can be written as

$$v_{dn} = -\mu_n \mathcal{E}, \tag{2.21}$$

where $\mu_n$ is proportional constant known as the mobility and $\mathcal{E}$ is the applied electric field.

Similarly, the drift velocity of the hole is

$$v_{dp} = \mu_p \mathcal{E}, \tag{2.22}$$

where $\mu_p$ is the hole mobility.

The total drift current density of holes and electrons is given by

$$J_{drf} = q\left(\mu_n n + \mu_p p\right)\mathcal{E}, \tag{2.23}$$

where $q$ is the electronic charge.

The mobility of carrier is closely associated with resistivity $\rho$ through the relation;

$$\rho = \frac{1}{q\left(\mu_n n + \mu_p p\right)}, \tag{2.24}$$

where $n$ and $p$ are the carrier number density. There is another case of motion, where the concentration gradient of carriers can create carrier diffusion and diffusion current. In a one-dimensional case, the diffusion current is proportional to the concentration gradient of the carriers as

$$J_{diff} = -qD\frac{dN(x)}{dx}, \tag{2.25}$$

where $D$ is the diffusion coefficient of the carrier, and $N(x)$ is the number density at position $x$. From Einstein relation, the diffusion coefficient can be written as [9]

$$\frac{D_n}{\mu_n} = \frac{D_p}{\mu_p} = \frac{kT}{q}, \tag{2.26}$$

where $D_n$ and $D_p$ are the electron and the hole diffusion coefficient, respectively.

## 2.4 The pn-Junction [11]

When p-type and n-type semiconductors are brought together into contact, there is a distortion of energy band at the interface. This is called the pn-junction. The pn-junction provides many characteristics distinguishing from a single piece of semiconductor. One important characteristic is the rectifying behavior as shown in Fig.2.1. Some semiconductor devices use this function to operate as such a diode.

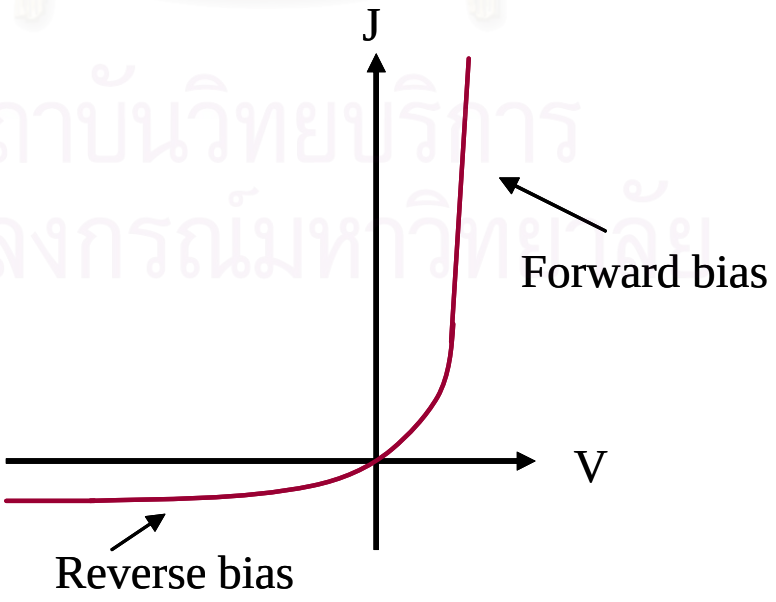


Figure 2.1: General curve of J-V characteristics of a pn-junction.

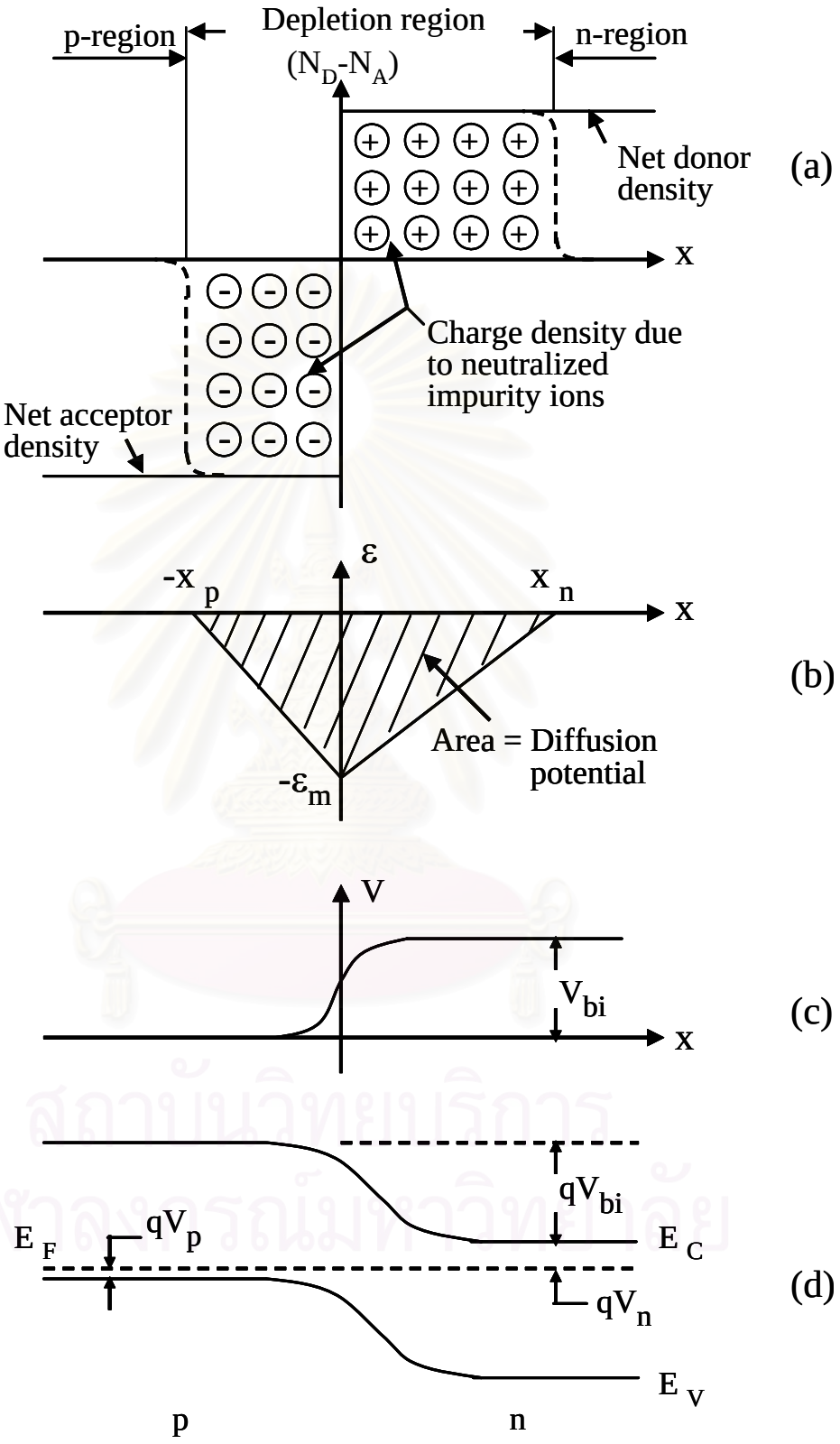


Figure 2.2: Abrupt pn-junction in thermal equilibrium: (a) Charge distribution at the junction interface (b) the magnitude of the electric field (c) potential variation with distance (d) energy band diagram [11].

At the junction, majority carriers or electrons in the n-region diffuse into the p-region and majority carriers or holes in the p-region diffuse into the n-region. This diffusion process makes a charge imbalance on both sides of the junction. The net positive and negative charges in the n-region and the p-region, respectively, create an electric field, which directs from the n-region to the p-region. The net positive and negative regions are referred as the space charge region or the depletion region. The electric field sweeps all electrons and all holes out of the space charge region and reach the thermal equilibrium. Several conditions at the junction are shown in Fig.2.2, where $V_{bi}$ is built-in voltage. The quantities $x_n$, $x_p$ and the electric field magnitude may be derived by applying Poisson's equation to the interface region.

From the use of some conditions such as constant doping concentration in each region, low injection of minority carrier across the junction, minority carrier concentration related to Boltzmann approximation and no generated current existing at the junction, the current-voltage relation of the pn-junction can be written as

$$J = J_s \left[ \exp\left(\frac{qV}{kT}\right) - 1 \right]. \tag{2.27}$$

The reverse saturation current $J_s$ is

$$J_s = \frac{qD_p p_{no}}{L_p} + \frac{qD_n n_{po}}{L_n}, \tag{2.28}$$

where $p_{no}$ and $n_{po}$ are the minority carrier density in equilibrium. Equation (2.27) with (2.28) is known as the ideal diode equation.

## 2.5 The Heterojunction [9,11-12]

The heterojunction is defined as the junction of two semiconductors with different energy band gap are brought into contact. The energy band will show a discontinuity at the junction interface. By considering different semiconductors on either side of the junction including n-p and p-n heterojunctions, the junction is called

anisotype heterojunction. The heterojunction should not have interface states. The interface state is due to the effect of dislocation between the two materials, being resulted from three main factors such as lattice mismatch, thermal mismatch and interdiffusion [2]. Using Anderson's model [2], an abrupt pn-heterojunction are described in Fig.2.3.

The subscripts "1" and "2" refer to n-type and p-type, respectively. It is assumed that the effect of dipoles and interface states is neglected. The spike in the conduction band is a barrier to the photo-generated electrons from the p-type when the junction is used as a solar cell. They will pile up at $x = 0$ and then recombine, therefore reducing the photo-generated current of the device. The two materials, in sensual, have different energy band gaps, different permittivities $\epsilon$, different work functions $\phi$, and different electron affinities $\chi$. The work function and electron affinity are referred to the energy required to remove the electron from the Fermi level and from the bottom of the conduction band, respectively, to vacuum.

The discontinuity in the conduction band edge is denoted by $\Delta E_C$ and that in the valence band edge by $\Delta E_V$. Figure 2.3(a) also shows that

$$\Delta E_C = q(\chi_2 - \chi_1). \tag{2.29}$$

When a junction is formed between these semiconductors, the energy band profile at equilibrium is shown in Fig.2.3(b). The discontinuity in the conduction band edge and the valence band edge is invariant with doping where $E_g$ and $\chi$ are not functions of doping, i.e., nondegenerate semiconductors, because the Fermi level must coincide on both sides in equilibrium and the continuous vacuum level is everywhere parallel to the band edges. However, $\Delta E_C$ and $\Delta E_V$ must be zero for a homojunction.

The partial built-in voltage in the martial 1, $V_{b1}$, and that in the material 2, $V_{b2}$, are the electrostatic potential required to equate the Fermi level across the

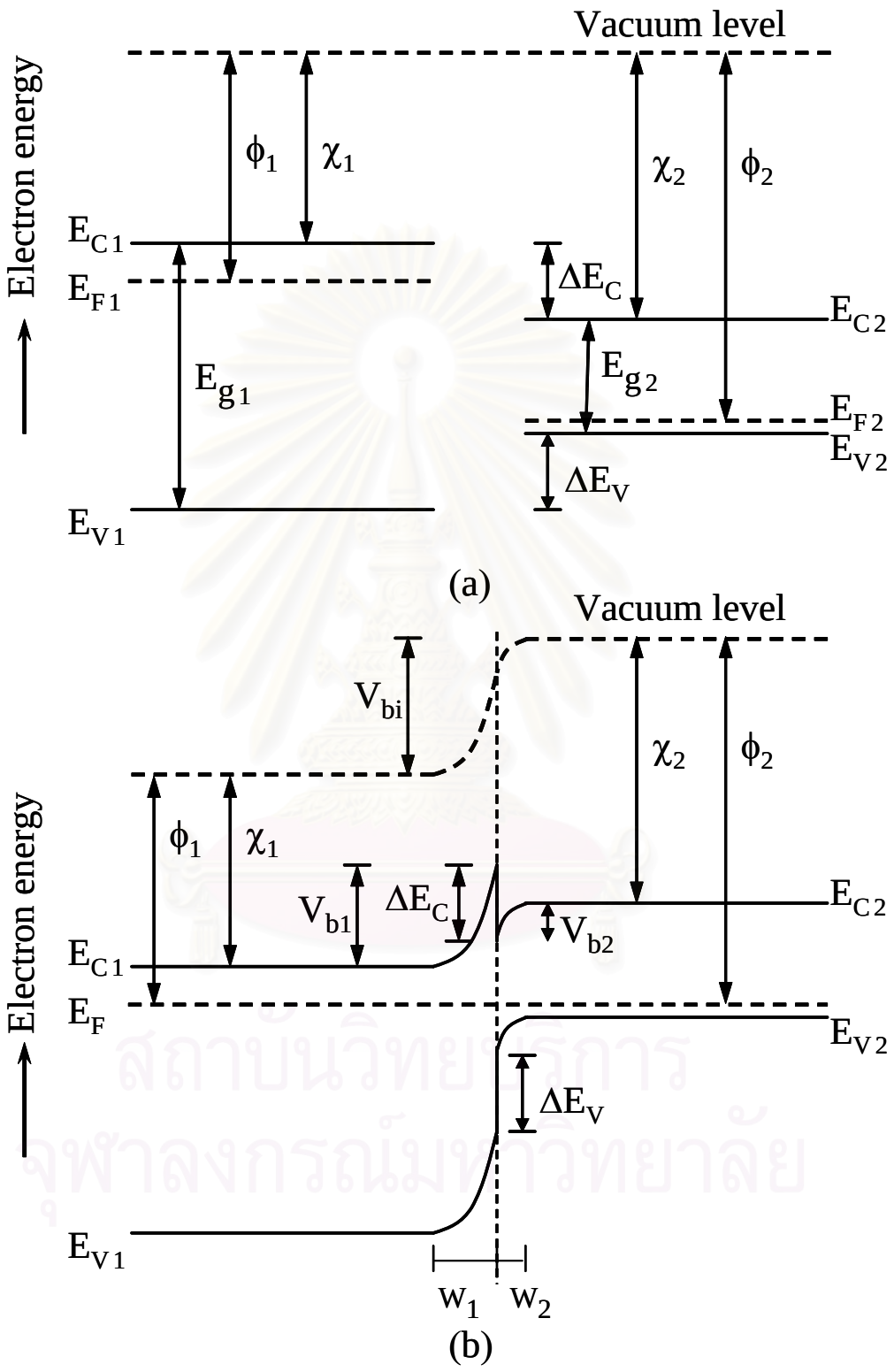


Figure 2.3: Equilibrium energy band diagrams before (a) and after (b) the formation of an abrupt n-p hetertojunction which has the conduction band spike [2].

junction interface. The total built-in voltage $V_{bi}$ is the sum of $V_{b1}$ and $V_{b2}$. It is also due to the difference between the work functions, or

$$V_{bi} = \phi_2 - \phi_1. \tag{2.30}$$

From Fig.2.3, Equation (2.30) can be rewritten as [9]

$$qV_{bi} = [q\chi_2 + E_{g2} - (E_{F2} - E_{V2})] - (q\chi_1 + E_{C1} - E_{F1}). \tag{2.31}$$

The electric field can be determined from Poisson's equation. We have in the n-type:

$$\mathcal{E} = \frac{eN_D(x + W_1)}{\epsilon_1} \qquad \text{at } -W_1 \le x \le 0 \tag{2.32}$$

and in the p-type:

$$\mathcal{E} = \frac{eN_A(W_2 + x)}{\epsilon_2} \qquad \text{at } 0 \le x \le W_2, \tag{2.33}$$

where $\epsilon_1$ and $\epsilon_2$ are the permittivities of the n-type and p-type, respectively. Because of the abrupt junction, the electric field is zero at the edge of the space charge region. The electric flux density is continuous across the junction, thus

$$\epsilon_1 \mathcal{E}(x = 0) = \epsilon_2 \mathcal{E}(x = 0), \tag{2.34}$$

giving

$$N_D W_1 = N_A W_2. \tag{2.35}$$

Equation (2.35) states that the net positive charge in the n-type must be equal to that in the p-type.

The integration of the electric field through the space charge region gives the partial built-in voltages in both regions, so we have

$$V_{b1} = \frac{eN_D W_1^2}{2\epsilon_1} \tag{2.36}$$

and

$$V_{b2} = \frac{eN_A W_2^2}{2\epsilon_2}. \tag{2.37}$$

The maximum electric field in the junction interface ($x = 0$) is

$$\mathcal{E}_{max} = \frac{eN_D W_1}{\epsilon_1} = \left[\frac{2eN_D V_{b1}}{\epsilon_1}\right]^{\frac{1}{2}} \tag{2.38}$$

or

$$\mathcal{E}_{max} = \frac{eN_A W_2}{\epsilon_2} = \left[\frac{2eN_A V_{b2}}{\epsilon_2}\right]^{\frac{1}{2}}. \tag{2.39}$$

The ratio of the partial built-in voltages of each region can be written as

$$\frac{V_{b1}}{V_{b2}} = \frac{\epsilon_2 N_D W_1^2}{\epsilon_1 N_A W_2^2} = \frac{\epsilon_2 N_A}{\epsilon_1 N_D}. \tag{2.40}$$

The total built-in voltage is

$$V_{bi} = \frac{eN_D W_1^2}{2\epsilon_1} + \frac{eN_A W_2^2}{2\epsilon_2}. \tag{2.41}$$

The depletion width on each side can be found from Eqs.(2.35) and (2.41). We obtain

$$W_1 = \left[\frac{2N_A \epsilon_1 \epsilon_2 V_{bi}}{eN_D\,(\epsilon_2 N_A + \epsilon_1 N_D)}\right]^{\frac{1}{2}} \tag{2.42}$$

in the n-region and

$$W_2 = \left[\frac{2N_D \epsilon_1 \epsilon_2 V_{bi}}{eN_A\,(\epsilon_2 N_A + \epsilon_1 N_D)}\right]^{\frac{1}{2}} \tag{2.43}$$

in the p-region.

If the junction is biased by an external voltage $V$, the same equations apply by replacing $V_{bi}$ with $V_{bi} - V$, $V_{b1}$ with $V_{b1} - V_1$ and $V_{b2}$ with $V_{b2} - V_2$ as $V = V_1 + V_2$.

# CHAPTER 3

# Solar Cells

After discussing the basic idea of semiconductors and pn-junctions, the aim of this chapter is to introduce solar cells. Solar cells are semiconductor devices, which can convert sunlight into electrical power. Then, solar cells are considered as potentially alternative energy sources. In this chapter, we will describe the operation of solar cells, solar cell parameters, and heterojunction solar cells.

## 3.1 Solar Cell Operation

Consider solar cells under illumination shown in Fig.3.1. When photons with energy equal to or greater than the band gap enter the cells, some photons are absorbed within the material. On the other hand, photons with energy less than the band gap pass through the material and are not used for producing electricity. The photon energy absorbed in the material is transferred to the semiconductor. The photons with enough energy knock electrons loose, thus creating electron-hole pairs throughout the cell. Electrons and holes can diffuse to the depletion region or space charge region in which an electric field exits from the n-type to the p-type. The electric field sweep holes into the p-type and electrons to into the n-type. As a result, electric voltage and current occur and are fed out to an external circuit.

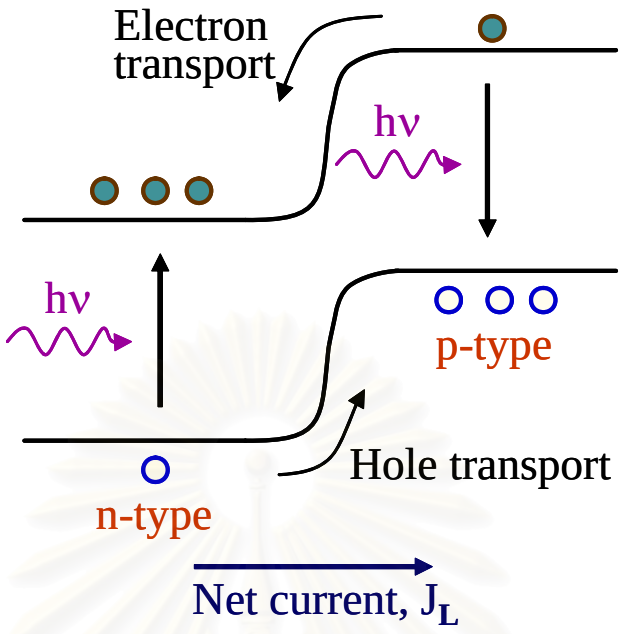


Figure 3.1: The transport of excess minority carriers in both regions of the solar cell under illumination that creates the net current with its direction from the n-region to the p-region [13].

## 3.2 Equivalent Circuits

For ideal solar cells, the simplest equivalent circuit [14] is shown in Fig.3.2, where $J_L$ is the photo-generated current which is opposite in direction to the diode current $J_d$ under forward bias. The equation used to explain Fig.3.2 is given by

$$J = J_s \left(e^{qv/AkT} - 1\right) - J_L, \tag{3.1}$$

where "A" is the diode ideality factor which is determined by the recombination current taking place during the photovoltaic operation and $J_s$ is the reverse saturation current. The first term of the right hand side of Eq.3.1 is also called diode current $J_d$.

We must also consider additional losses due to a non-negligible series resistance $R_s$ and a finite shunt resistance $R_{sh}$ for non-ideal solar cells. Incorporating these losses, the above equation becomes

$$J = J_s \left[\exp\left(\frac{qV}{AkT}\right) - 1\right] + \left(\frac{V - JR_s}{R_{sh}}\right) - J_L \tag{3.2}$$

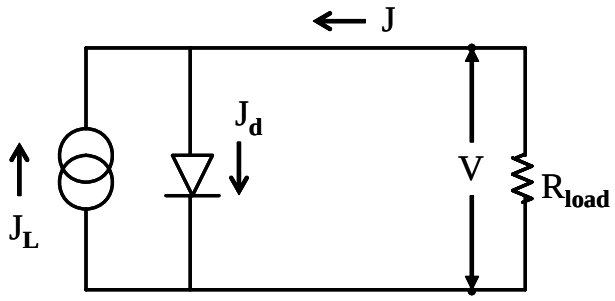


Figure 3.2: The equivalent circuit of an ideal solar cell.

Figure 3.3 shows an equivalent circuit according to Eq.(3.2). The existence of the shunt resistance is due to the loss caused by surface leakage along the edges of the cell, by diffusion spikes along dislocations of grain boundaries, or possibly by fine metallic bridges along micro cracks, grain boundaries, or crystal defects such as stacking faults. The series resistance takes place from contact resistance to the front and back, the resistance of the base itself and especially the sheet resistance of the front region layer.

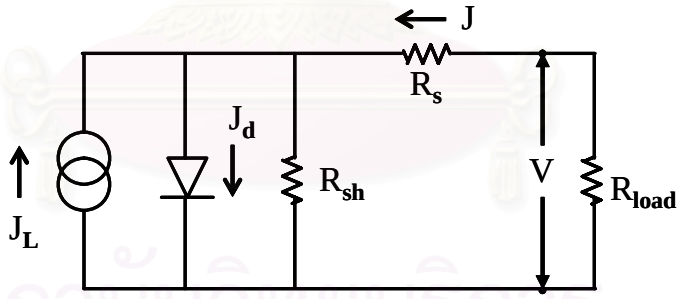


Figure 3.3: The equivalent ciruit of a non-ideal solar cell.

## 3.3 Output Parameters

Four parameters used to specify the performance of solar cells are short circuit current, open circuit voltage, fill factor, and efficiency. The current-voltage characteristics under illumination shown in Fig.3.4 is used to obtain these parameters. The short circuit current $J_{sc}$ is the current at zero voltage when the load resistance is 0 $\Omega$. The open circuit voltage $V_{oc}$ is the voltage at zero current when the load

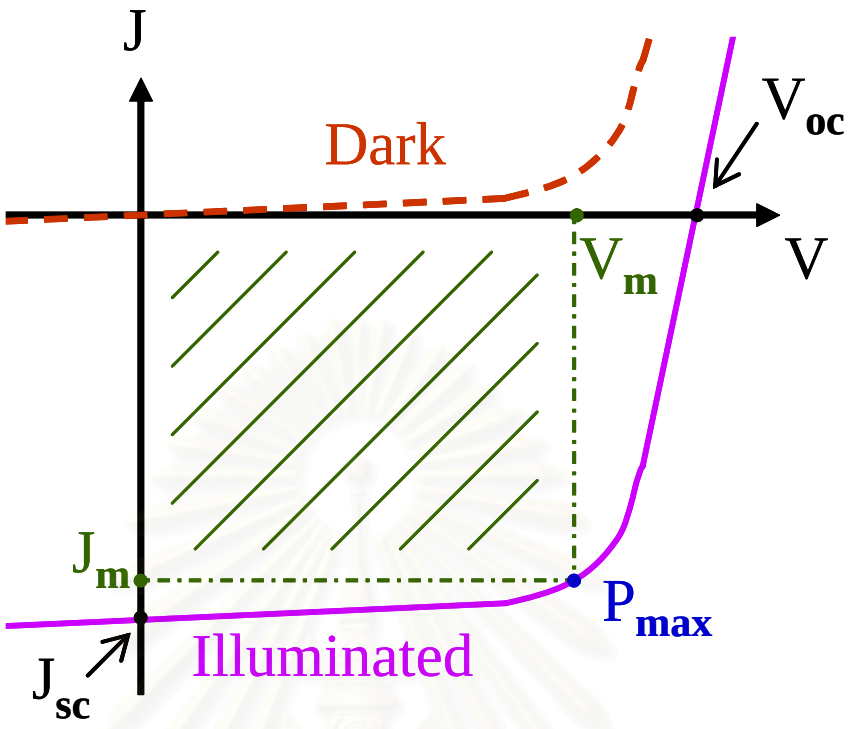


Figure 3.4: J-V characteristics of a solar cell in the dark and under illumination with important parameters.

resistance is very high. Inside the current-voltage curve, the maximum square area represents the maximum power output at $(J_m, V_m)$. The fill factor FF is the ratio of the maximum power output to the product of $J_{sc}$ and $V_{oc}$ as

$$FF = \frac{P_{max}}{J_{sc} V_{oc}} = \frac{J_m V_m}{J_{sc} V_{oc}}, \tag{3.3}$$

where the subscript "m" represents the current and voltage at the maximum output. Lastly, the efficiency $\eta$ of solar cells is the ratio of the maximum power output to the incoming power of light $P_{in}$ as

$$\eta = \frac{P_{max}}{P_{in}}. \tag{3.4}$$

In general, the efficiency is calculated at standard illumination or air mass 1.5 (AM 1.5) illumination which is demonstrated in Fig.3.5. Air mass 1.5 condition (cloudless sun at 45° above the earth surface at sea level) is the energy-weighted average for the terrestrial use and its magnitude is about 1,000 W/m$^2$.

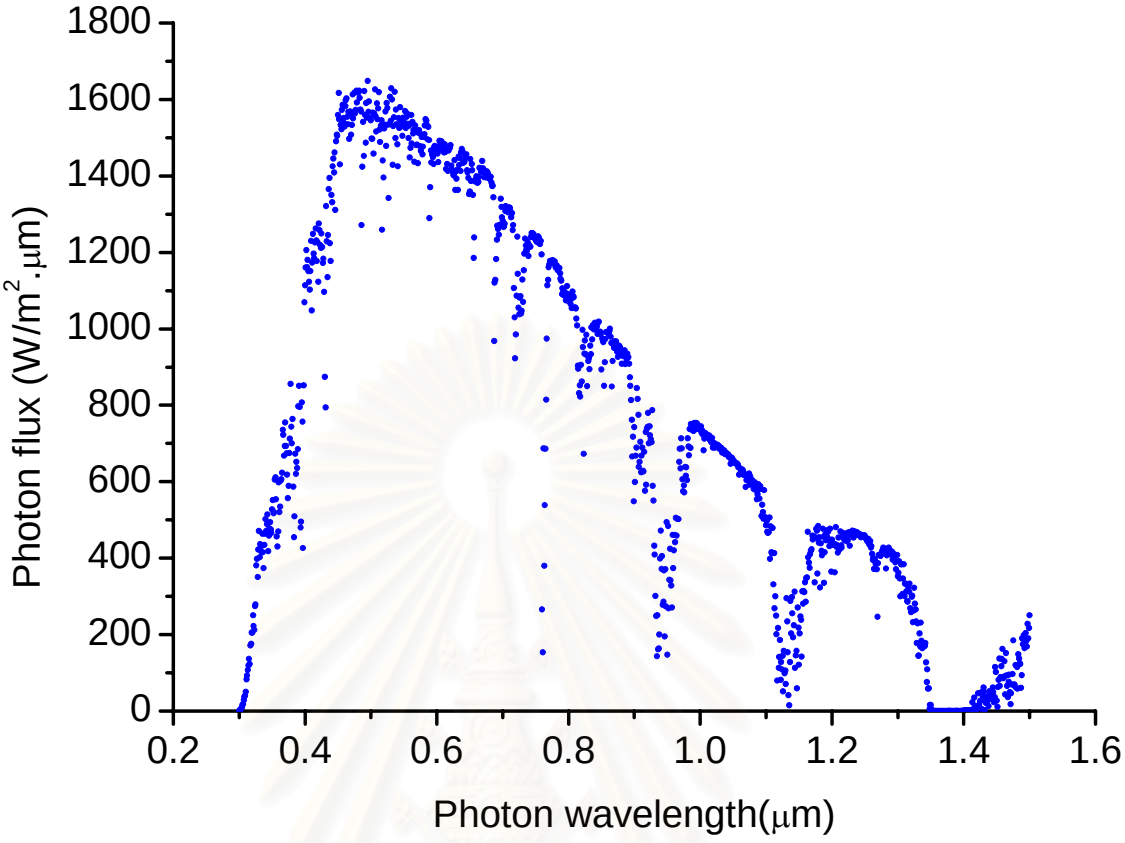


Figure 3.5: Photon flux in sunlight according to AM 1.5 [15].

## 3.4 Photo-Generated Current

When a beam of light with wavelength $\lambda$ strikes on the top of solar cells, the photo-generated current can be described as follows. The generation rate of electron-hole pairs as a function of distance $x$ from the cell surface and wavelength $\lambda$ is shown in Fig.3.6(a) and is given by [11]

$$G(\lambda, x) = \alpha(\lambda)F(\lambda)[1 - R_i(\lambda)] \exp[-\alpha(\lambda)x], \tag{3.5}$$

where $\alpha(\lambda)$ is the absorption coefficient, $F(\lambda)$ the number of incident photons /cm$^2$/s per unit bandwidth, and $R_i(\lambda)$ the fraction of these photons reflected from the surface. For low injection condition, the continuity equations of minority carrier are [14]

$$G_n - \frac{n_p - n_{po}}{\tau_n} + \frac{1}{q}\frac{dJ_n}{dx} = 0 \tag{3.6}$$

for electron in p-type semiconductor and [14]

$$G_p - \frac{p_n - p_{no}}{\tau_p} - \frac{1}{q}\frac{dJ_p}{dx} = 0 \tag{3.7}$$

for hole in n-type semiconductor. The current equations are

$$J_n = q\mu_n n_p \mathcal{E} + qD_n \frac{dn_p}{dx} \tag{3.8}$$

and

$$J_p = q\mu_p p_n \mathcal{E} - qD_p \frac{dp_n}{dx}, \tag{3.9}$$

where $p_n$ and $n_p$ are the photo-generated minority carrier densities.

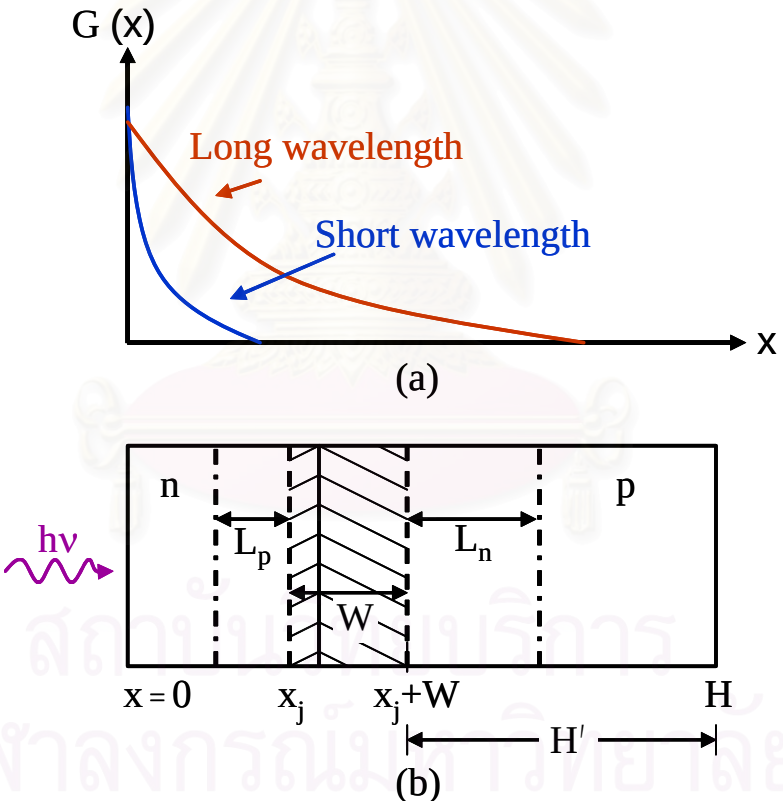


Figure 3.6: (a) Generation rate of electron-hole pairs as a function of distance into the cell. (b) Dimensions in a solar cell with minority-carrier diffusion lengths [11].

In case of a pn-junction with constant doping, there is no electric field outside the depletion region or shaded area in Fig.3.6(b). If the device is a junction that n-type is at the top and p-type is the base, Eqs.(3.6),(3.7) and (3.9) can be

combined as

$$D_p \frac{d^2 p_n}{dx^2} + \alpha F(1 - R_i) \exp(-\alpha x) - \frac{p_n - p_{no}}{\tau_p} = 0 \tag{3.10}$$

for the top side of the junction. The general solution to Eq.(3.10) is

$$p_n - p_{no} = A \cosh\left(\frac{x}{L_p}\right) + B \sinh\left(\frac{x}{L_p}\right) - \frac{\alpha F(1 - R_i)\tau_p}{\alpha^2 L_p^2 - 1} \exp(-\alpha x), \tag{3.11}$$

where $L_p$ is the diffusion length, $L_p = \sqrt{D_p \tau_p}$ . These two boundary conditions for Eq.(3.11). At the surface ($x = 0$), recombination with a recombination velocity $S_p$ takes place:

$$D_p \frac{d(p_n - p_{no})}{dx} = S_p (p_n - p_{no}). \tag{3.12}$$

At the depletion edge($x = x_j$), there is no excess minority carrier due to the electric field:

$$p_n - p_{no} \simeq 0. \tag{3.13}$$

Using these boundary conditions with Eq.(3.11), the hole density becomes

$$p_n - p_{no} = \left[\frac{\alpha F(1 - R_i)\tau_p}{\alpha^2 L_p^2 - 1}\right] \times$$

$$\left\{ \frac{\left(\frac{S_p L_p}{D_p} + \alpha L_p\right) \sinh\left(\frac{x_j - x}{L_p}\right) + e^{-\alpha x_j}\left[\frac{S_p L_p}{D_p} \sinh\left(\frac{x}{L_p}\right) + \cosh\left(\frac{x}{L_p}\right)\right]}{\frac{S_p L_p}{D_p} \sinh\left(\frac{x_j}{L_p}\right) + \cosh\left(\frac{x_j}{L_p}\right)} - e^{-\alpha x} \right\}. \tag{3.14}$$

Then, the photo generated current of the hole per unit bandwidth at the junction edge is

$$\begin{aligned} J_p &= -qD_p \left(\frac{dp_n}{dx}\right)_{x_j} \\ &= \left[\frac{qF(1 - R_i)\alpha L_p}{\alpha^2 L_p^2 - 1}\right] \times \\ &\quad \left\{ \frac{\left(\frac{S_p L_p}{D_p} + \alpha L_p\right) - e^{-\alpha x_j}\left[\frac{S_p L_p}{D_p} \cosh\left(\frac{x_j}{L_p}\right) + \sinh\left(\frac{x_j}{L_p}\right)\right]}{\frac{S_p L_p}{D_p} \sinh\left(\frac{x_j}{L_p}\right) + \cosh\left(\frac{x_j}{L_p}\right)} - \alpha L_p e^{-\alpha x_j} \right\}. \end{aligned} \tag{3.15}$$

This current would be collected by assuming uniform lifetime, mobility and doping level. The electron photo-generated current collected from the base is derived by using Eqs.(3.5),(3.6) and (3.8) with two boundary conditions such as

$$n_p - n_{po} \simeq 0 \qquad \text{at} \qquad x = x_j + W \tag{3.16}$$

and

$$S_n\,(n_p - n_{po}) = -D_n \frac{dn_p}{dx} \qquad \text{at} \qquad x = H, \tag{3.17}$$

where $W$ is the depletion width and $H$ the width of the entire cell. The electron density in a uniform base is

$$\begin{aligned} n_p - n_{po} = {} & \left[\frac{\alpha F(1-R_i)\tau_n}{\alpha^2 L_n^2 - 1}\right] \exp\left[-\alpha\,(x_j + W)\right] \times \\ & \left\{\cosh\left(\frac{x - x_j - W}{L_n}\right) - e^{-\alpha\left(x - x_j - W\right)}\right. \\ & - \frac{\left(\frac{S_n L_n}{D_n}\right)\left[\cosh\left(\frac{H'}{L_n}\right) - \exp\left(-\alpha H'\right)\right] + \sinh\left(\frac{H'}{L_n}\right) + \alpha L_n e^{-\alpha H'}}{\left(\frac{S_n L_n}{D_n}\right)\sinh\left(\frac{H'}{L_n}\right) + \cosh\left(\frac{H'}{L_n}\right)} \\ & \left. \times \sinh\left(\frac{x - x_j - W}{L_n}\right)\right\}. \end{aligned} \tag{3.18}$$

Hence, the photo-generated current of the electron at the depletion edge, $x = x_j + W$, is

$$\begin{aligned} J_n &= qD_n \left(\frac{dn_p}{dx}\right)_{x_j + W} \\ &= \left[\frac{qF\,(1-R_i)\,\alpha L_n}{\alpha^2 L_n^2 - 1}\right] \exp\left[-\alpha\,(x_j + W)\right] \\ & \left\{\alpha L_n - \frac{\left(\frac{S_n L_n}{D_n}\right)\left[\cosh\left(\frac{H'}{L_n}\right) - e^{-\alpha H'}\right] + \sinh\left(\frac{H'}{L_n}\right) + \alpha L_n e^{-\alpha H'}}{\left(\frac{S_n L_n}{D_n}\right)\sinh\left(\frac{H'}{L_n}\right) + \cosh\left(\frac{H'}{L_n}\right)}\right\}, \end{aligned} \tag{3.19}$$

where $H'$ shown in Fig.3.6(b) is the total cell thickness minus the junction depth and the depletion width, $H' = H - (x_j + W)$.

There are the other photo-generated current taking place at the depletion region, where the electric field is high enough to separate photo-generated carriers out of this region before they recombine again. The photo-generated current per unit bandwidth is equal to the number of photons absorbed as

$$J_{dr} = qF(1 - R_i)\exp(-\alpha x_j)\left[1 - \exp(-\alpha W)\right]. \tag{3.20}$$

The total photo-generated current at a given wavelength is the sum of Eqs.(3.15), (3.19) and (3.20):

$$J_L(\lambda) = J_p(\lambda) + J_n(\lambda) + J_{dr}(\lambda). \tag{3.21}$$

The spectral response (SR) or quantum efficiency (QE) can be written as

$$SR(\lambda) = \frac{J_L(\lambda)}{qF(\lambda)}. \tag{3.22}$$

## 3.5 Heterojunction Solar Cells

Heterojunction are junctions, which consist of semiconductors with different energy gaps. For a typical n-on-p heterojunction, the semiconductor with large energy gap $E_{g1}$which acts like a window is on the semiconductor with smaller energy gap $E_{g2}$ as shown in Fig.2.3. Light with energy less than $E_{g1}$ but greater than $E_{g2}$ can pass through the first semiconductor and be absorbed by the second semiconductor. This light creates carriers in the depletion region and within the diffusion length of the junction. Light with energy greater than $E_{g1}$ is absorbed by the first semiconductor thus making carriers in the depletion region and within the diffusion length from the junction. The equation, which explains the photo generated current in the heterojunction, is similar to that in the homojunction. For n-on-p junction, the hole photo-generated current in the first semiconductor is given by Eq.(3.15) but $\alpha$ is replaced by $\alpha_1$ and $L_p$ by $L_{p1}$, where $\alpha_1$ and $L_{p1}$ are the absorption coefficient and diffusion length in the first semiconductor, respectively. The electron photo-generated current is given by Eq.(3.19) but $\alpha$ is replaced by $\alpha_2$, $L_n$ by $L_{n2}$

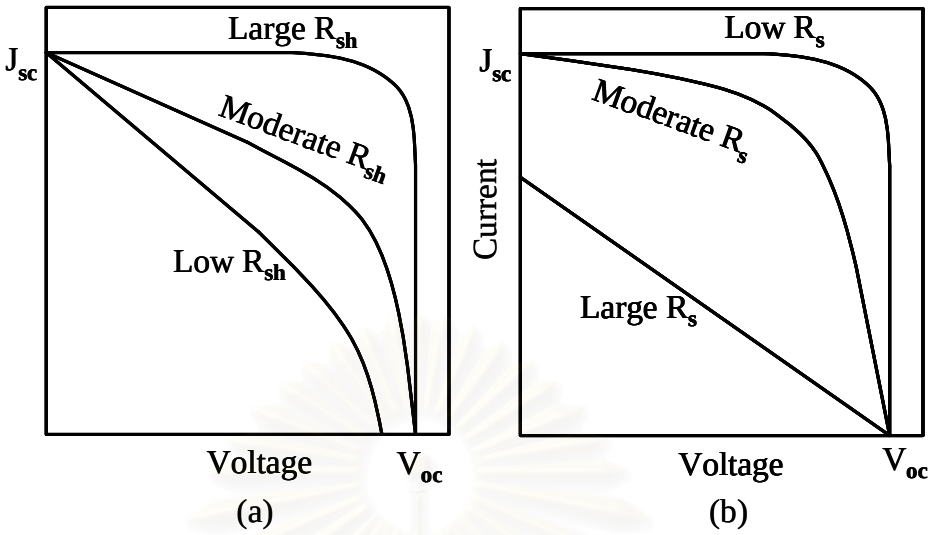


Figure 3.7: Effect of parasitic resistors on the output parameters of solar cells: (a) effect of shunt resistance (b) effect of series resistance [1].

and $\alpha(x_j + W)$ by $[\alpha_1(x_j + W_1) + \alpha_2 W_2]$, where $\alpha_2$ and $L_{n2}$ are the absorption coefficient and diffusion length in the second semiconductor, respectively. The photo-generated current in the depletion region is expressed by [11]

$$J_{dr} = qF(1 - R_i)\left[e^{-\alpha_1 x_j}\left(1 - e^{-\alpha_1 W_1}\right) + e^{-\alpha_1(W_1 + x_j)}\left(1 - e^{-\alpha_2 W_2}\right)\right]. \qquad (3.23)$$

The expressions are valid when small conduction discontinuity $\Delta E_C$ (in the case of p-on-n heterojunction, $\Delta E_V$ should be small) and heterojunction with good lattice match are considered, so minority carriers in the second semiconductor will not be dropped from flowing across the junction.

## 3.6 The Effect of Resistances

The equivalent circuit of solar cells shows that there are two types of resistance, which affect the output parameters of solar cells. Figure 3.7(a) shows the effect of shunt resistance. Shunt resistance does not affect the short circuit current but the fill factor and open circuit voltage are reduced when the shunt resistance decreases. The influence of the shunt resistance is more obvious at low solar intensities and low temperatures [1]. Figure 3.7(b) shows the effect of series resistance. The open

circuit voltage is not affected but the fill factor and short circuit current decreases as the series resistance builds up. On the other hand, the series resistance becomes more important at high intensities and high temperatures. In general, solar cells must have high shunt resistance and low series resistance to avoid the low value of fill factor, thus afterwards influencing the efficiency [1]. The way, which lessens the series resistance, is to make high doping level, deep junctions and optimizing the design of front contact grid.

## 3.7 Top Contact Design

The optimization of top contact design [1] is an important requirement to obtain the high efficiency of solar cells. It is increasingly more important as the area of the solar cell increases [16]. There is an optimal shape design of one front-contact grid for small-size unit cell by investigating some parameters such as sheet resistance of the top layer and the maximized area disclosed to incident light. In a simple model, the direction of current is perpendicular to the surface of the top layer in the bulk of the junction but lateral in the top layer (see Fig.3.8). For example, the unit cell of the solar cell has length $L$ and arbitrary shape. The functions $g(y)$ and $f(y)$ describe solar cell boundary shape and grid shape, respectively, where $y$

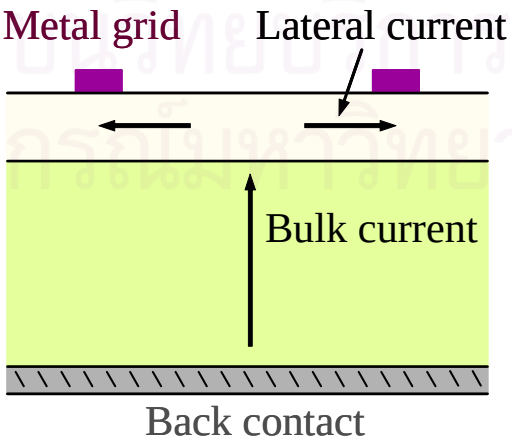


Figure 3.8: Direction of current flow in each region of a pn-junction solar cell [1].

directs on the longitudinal axis of the grid. At the position $y$, the current is [1]

$$i(y) = \int_0^y J_L \left[ g(\xi) - f(\xi) \right] \, d\xi. \tag{3.24}$$

The power loss due to grid sheet resistance is

$$PL = \int_0^L \rho_g \left[ \frac{i(y)^2}{f(y)} \right] \, dy, \tag{3.25}$$

where $\rho_g$ is resistivity of the grid.

Optimal grid shape is accomplished when the $PL$ is minimized. The grid will be semi-taper shape if the function $g(y)$ is a constant value (rectangular unit cell). In fact, the thin film solar cells are fabricated mostly in rectangular shape.

In addition, for larger cell with rectangular shape, only optimal front-contact grid is not sufficient to accept current from expanding cell, which caused by widely exposing to light. Thus, the alignment of many optimal grids in terms of the spacing between grids must be investigated. The power loss mechanisms at the front-contact grid such as top layer sheet resistance, grid sheet resistance, grid shadowing and contact resistance between grid and top layer are also used to determine the grid spacing. The fractional power loss caused by top layer sheet resistance is [1]

$$p_t = \frac{\rho_t J_m S^2}{12 V_m}, \tag{3.26}$$

where $\rho_t$ and $S$ are top layer sheet resistance and grid spacing, respectively. The fraction power loss in the grids is [1]

$$p_g = \frac{B_F^2 \rho_g J_m S}{m V_m W_F}, \tag{3.27}$$

where $B_F$ and $W_F$ are the width of top layer and average grid width, respectively. The parameter $m$ is 4 if each grid is taper and 3 for uniform width. The fractional power loss caused by grid shadowing is [1]

$$p_s = \frac{W_F}{S}. \tag{3.28}$$

Finally, the fractional power loss of contact resistance between grid and top layer is [1]

$$p_c = \frac{\rho_c J_m S}{V_m W_F}, \tag{3.29}$$

where $\rho_c$ is contact resistivity.

To investigate the value of $S$, the sum of Eqs.(3.26) to (3.29) are calculated by a simple iterative method. The optimum occurs when the efficiency loss caused by each fraction becomes as small as possible. A quantity for describing the series resistance of the top layer is the sheet resistance, which is the resistivity divided by the layer thickness. The sheet resistance has the dimension of Ohm but is commonly expressed as Ohm/square or $\Omega/\square$.

## 3.8 Cu(In,Ga)$Se_2$-Based Solar Cells

The state-of-the-art solar cells based on Cu(In,Ga)$Se_2$ or CIGS is the most promising candidates because of the highest efficiency of all thin film solar cells. Several research groups have found that the maximum efficiency can be obtained as high as 19.2% on the laboratory scale [17] and 16.6% for mini-modules (19 $cm^2$) [18]. In addition, outdoor long-term stability and radiation harness are excellent issues for commercial uses [19]. The CIGS-based solar cell is a heterojunction with its standard structure shown in Fig.3.9; the structure consists of five thin layers deposited on a substrate and a metal grid at the top. The ZnO and CdS are usually n-type and the CIGS is p-type. The junction is considered to form at or near the CdS/CIGS interface. The CIGS is a direct band gap semiconductor, and is used as an absorber layer. The absorber layer is initially made from pure $CuInSe_2$ but can be partially replaced In with Ga, thus the band gap can be adjusted from 1.04 eV to 1.2 eV [19] for the best solar cell. Schock *et al* [19] presented the band diagram of the CIGS-based solar cell as shown in Fig.3.10 with an applied bias voltage $V$. $E_{Fn}$ and $E_{Fp}$ are the Fermi level energies for electrons and holes, respectively.

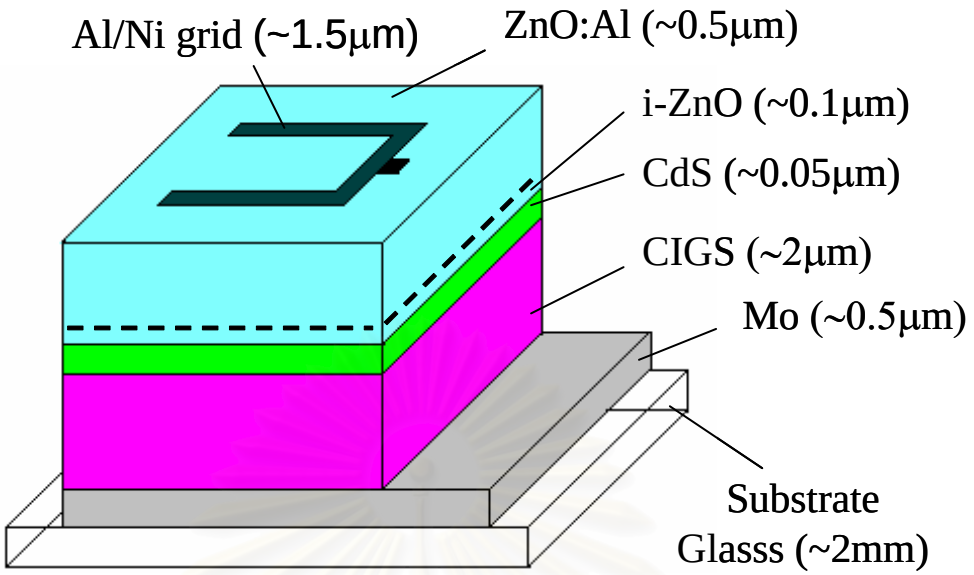


Figure 3.9: The different layers of a ZnO/CdS/CIGS solar cell [13].

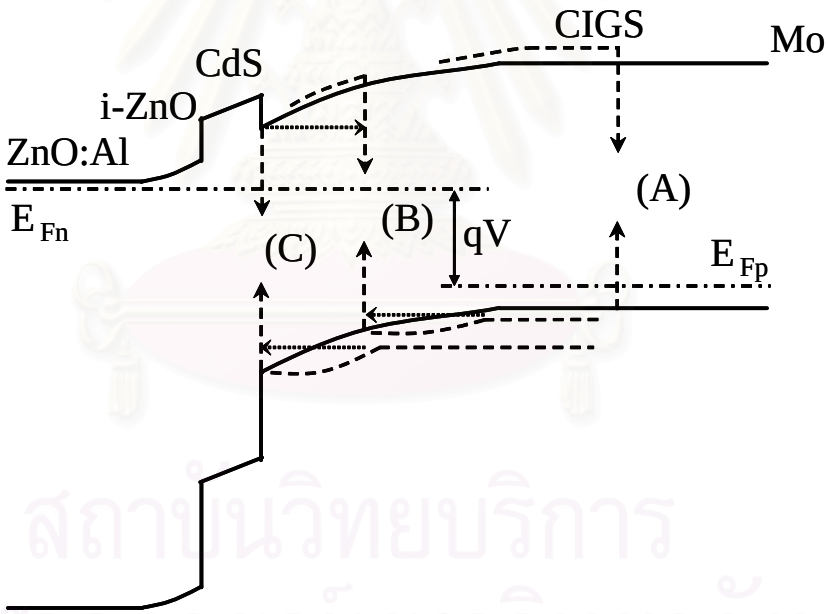


Figure 3.10: Energy band diagram of a ZnO/CdS/CIGS solar cell under forward bias with three recombination paths, (A)-(C), and tunneling enhanced proceses, lateral dotted arrows [21,22].

Figure 3.10 also shows three relevant recombination paths, which are recombination in the neutral bulk (A), in the space-charge region (B) and at the CIGS/CdS interface (C). The horizontal dotted arrows indicate enhancement of the later two. For these three recombinations, the dark current (diode current)

can be described by [21]

$$J = J_s \left[ \exp\left(\frac{qV}{AkT}\right) - 1 \right]. \tag{3.30}$$

The reverse saturation current $J_s$ is given by [19]

$$J_s = J_{oo} \exp\left(\frac{-E_a}{AkT}\right), \tag{3.31}$$

where $E_a$ is the activation energy and $J_{oo}$ a prefactor. It is believed that the high-efficiency CIGS-based solar cell is dominated by recombination in the space-charge region. Then, the activation energy is close to the energy band gap. At open circuit condition, the dark current is equal to the $J_{sc}$ so that the net current is zero. Combining Eqs.(3.30) and (3.31), the open circuit voltage becomes

$$V_{oc} = \frac{E_a}{q} - \frac{AkT}{q} \ln\left(\frac{J_{oo}}{J_{sc}}\right). \tag{3.32}$$

If the temperature is reduced to 0 K, the plot of the $V_{oc}$ vs $T$ gives the activation energy.

In the temperature range between 350 and 200 K, the recombination is without tunneling. The diode ideality factor can be defined as [22]

$$\frac{1}{A} = \frac{1}{2}\left(1 + \frac{T}{T^*}\right), \tag{3.33}$$

where $kT^*$ is the characteristic energy of an exponential distribution of trap states.

At low temperature ($< 200K$), the tunneling is considered and the diode ideality factor is changed to be [22]

$$\frac{1}{A} = \frac{1}{2}\left(1 + \frac{T}{T^*} - \frac{E_{oo}^2}{3\,(kT)^2}\right) \tag{3.34}$$

with the characteristic tunneling energy $E_{oo}$. An example for Eqs.(3.33) and (3.34) is shown in Fig.3.11. The dash line describes recombination without tunneling according to Eq.(3.33). The full line agrees with Eq.(3.34) which explains the tunneling.

Dark and light curves of the CIGS-based solar cell exhibit cross over or non-superposition due to the modulation of the conduction band spike, thus affecting diode current of the cell. This is governed by electronic doping of deep level defect in the CdS buffer layer with white light or blue light soaking [23-27]. The J-V curve also becomes in the form of "s" like shape, namely red kink, which the slope of the curve decreases before reaching the open circuit, when the cell is kept in the illumination with only red light $>$ 600nm. The red kink happens since the excess electrons from the absorption of photons in the CIGS layer do not have sufficient energy in order to cross across this conduction band spike [28].

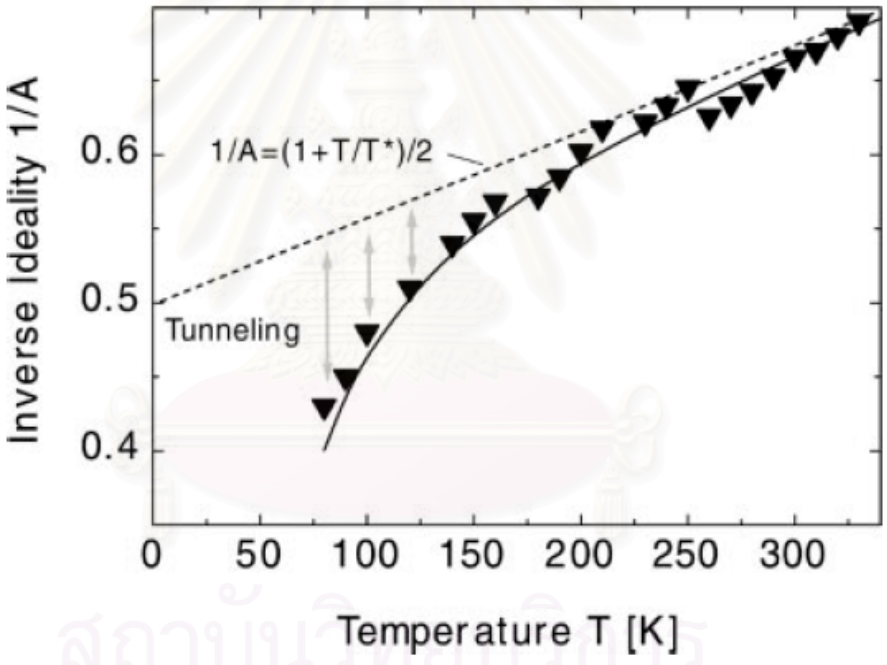


Figure 3.11: The temperature dependance of the inverse diode idealtiy factor of a ZnO/CdS/CIGS solar cell [19].

# CHAPTER 4

# Methodology

In this chapter, we briefly discuss the description of the calculation of the photocurrent, which is used later as one initial parameter. Then, the circuit model of the solar cell exposed to light is presented. The circuit model can also be used to explain the current-voltage (J-V) characteristics that we use to optimize the assumed grid patterns. In the final part of this chapter, we will explain the evaluation scheme concerning the procedure of JV-characteristic for finding the efficiency of the solar cell with each grid pattern.

## 4.1 Photocurrent Calculation

In order to calculate the photocurrent, we must know the parameters associated with the solar cells such as built-in voltage, depletion width and diffusion length. The built-in voltage is a value that the band diagram bends at the junction interface. In this study, we assume that the n-region consists of two layers, i.e. CdS and ZnO. Then, the p-region comprises CIGS. The junction interface is presumably appointed at the interface between CdS and CIGS. Using Eq.(2.31) where the subscript 1 and 2 refer to CdS and CIGS, respectively, together with material parameters in Table 4.1, the built-in voltage can be obtained. The value of $(E_{F2} - E_{V2})$ and $(E_{C1} - E_{F1})$ can be derived from Eqs.(2.17) and (2.18), respectively. Therefore, the value of the built-in voltage is 1.166 V.

The depletion width shows the width of band bending in each region of the junction. We use Eqs.(2.42) and (2.43), where $V_{bi}$ is replaced by $(V_{bi} - V)$ and $V$ is a bias voltage which varies from short circuit to open circuit, to find the depletion

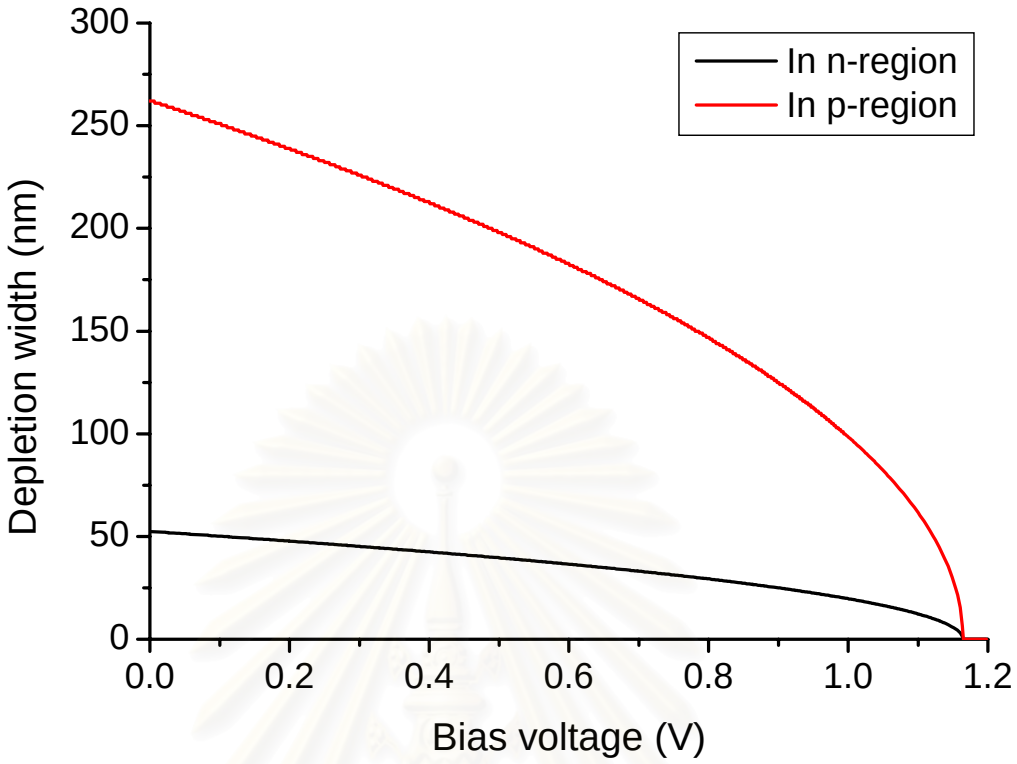


Figure 4.1: Calculated depletion width of each region for the junction.

width in each region of the junction as shown in Fig 4.1.

The depletion width in p-region is larger than that in n-region since the carrier density of CIGS is less than that of CdS. These depletion widths become eventually zero when the bias voltage is equal to the built-in voltage.

Besides, we must know the diffusion length of excess minority carrier of both regions. The diffusion length is the square root of the product of minority carrier lifetime, which is given by [11]

$$\tau = \frac{1}{\sigma N_{def}\sqrt{\frac{3kT}{m^*}}}, \tag{4.1}$$

where $\sigma$ is cross-section and $N_{def}$ is defect density, and diffusion coefficients previously shown in Eq.(2.26). In this calculation, effective masses are also assumed to be $m_e^* = 0.2m_0$ and $m_h^* = 0.8m_0$ [28], where $m_0$ is the rest mass of electrons. We can calculate the diffusion length by using parameters in Table 4.1. This yields excess minority holes in both ZnO and CdS, and electrons in CIGS as shown in

Table 4.2.

Table 4.1: Material parameters for the CIGS-based solar cell [29].

| **General properties** | | | |
|---|---|---|---|
| | | Front surface | Back surface |
| Surface recombination velocity | | $10^7$ cm/s | $10^7$ cm/s |
| Reflectivity | | 0.1 | - |
| **Layer properties** | | | |
| | ZnO | CdS | CIGS |
| Width | 0.5 μm | 50 nm | 2 μm |
| Dielectric constant | - | 10 | 13.6 |
| Excess carrier mobility | 25 $cm^2$/Vs | 25 $cm^2$/Vs | 100 $cm^2$/Vs |
| Carrier density | - | $10^{17}$ $cm^{-3}$ | $2\times10^{16}$ $cm^{-3}$ |
| Band gap | - | 2.4 eV | 1.12 eV |
| Effective density of states | - | $2.22\times10^{18}$ $cm^{-3}$ | $1.78\times10^{19}$ $cm^{-3}$ |
| Electron affinity | - | 3.8 eV | 4.1 eV |
| Defect density | $10^{17}$ $cm^{-3}$ | $10^{18}$ $cm^{-3}$ | $10^{14}$ $cm^{-3}$ |
| Cross-section | $10^{-17}$ $cm^2$ | $9.8\times10^{-13}$ $cm^2$ | $5.3\times10^{-13}$ $cm^2$ |

Table 4.2: Calculated parameters of each material.

| | ZnO | CdS | CIGS |
|---|---|---|---|
| Diffusion coefficient | 0.65 $cm^2$/s | 0.65 $cm^2$/s | 2.59 $cm^2$/s |
| Lifetime | $7.66\times10^{-8}$ s | $7.81\times10^{-14}$ s | $7.22\times10^{-10}$ s |
| Diffusion length | $2.22\times10^{-6}$ m | $2.25\times10^{-9}$ m | $4.32\times10^{-7}$ m |

By the end of this section, the important parameters have been completely prepared before starting the calculation for photocurrent. The n-region consists of two layers, i.e. CdS and ZnO. Hence, there are two conditions for the achievement for the photocurrent.

In the case of $x_j < W_{ZnO}$, the depletion region covers entirely in CdS and partially in both ZnO and CIGS, so the photocurrent in the depletion region differs from Eq.(3.23) and is given by

$$J_{dr} = qF(1 - R_i)\left[\exp(-\alpha_{ZnO}x_j) - \exp(-\alpha_{CdS}W_{CdS} - \alpha_{ZnO}W_{ZnO} - \alpha_{CIGS}W_2)\right], \tag{4.2}$$

where $W_{ZnO}$ and $W_{CdS}$ are the width of the ZnO layer and the CdS layer, respectively. It is caused by the fraction of incident photons absorbed by these three

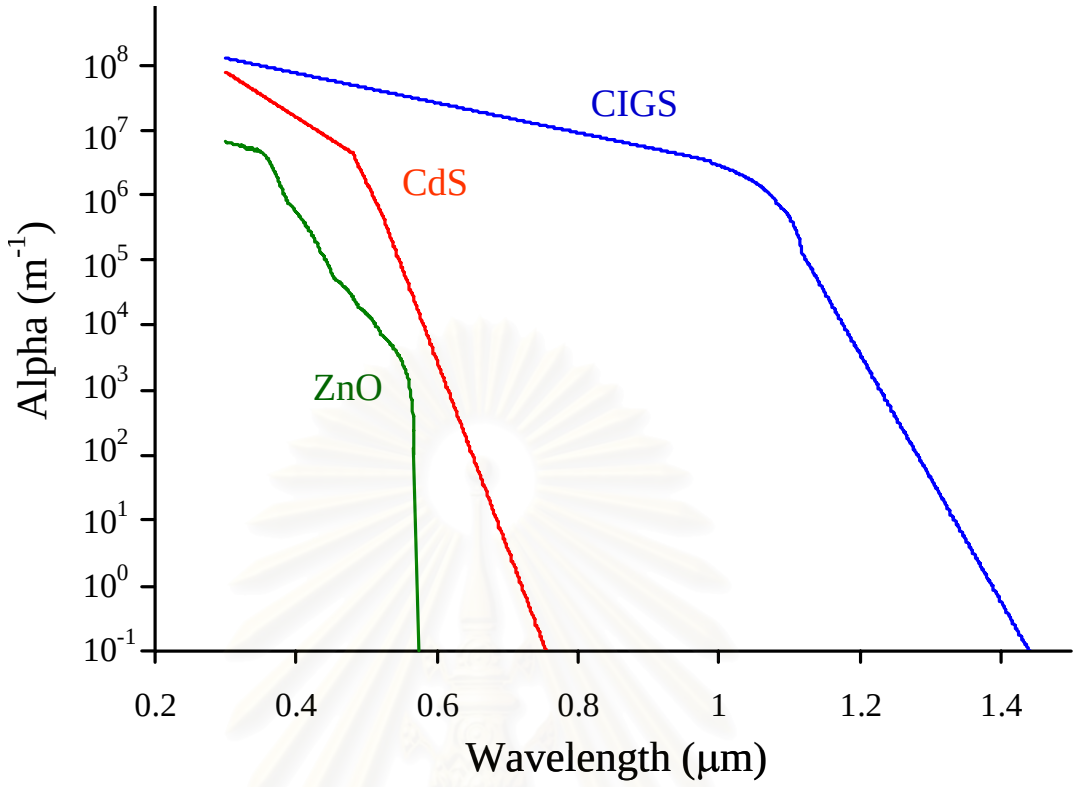


Figure 4.2: Absorption coefficient spectra for ZnO, CdS and CIGS [28].

layers, thus converting to current without recombination loss due to the electric field of the abrupt junction in this region. Figure 4.2 shows the absorption coefficient for ZnO $\alpha_{ZnO}$, CdS $\alpha_{CdS}$ and CIGS $\alpha_{CIGS}$. CIGS has the strong absorption coefficient in the range of wavelength less than 1.2 μm. Then, CIGS with 2.0 μm thick is sufficient to be used as the absorber and can absorb entirely remaining photons from over layers. The photocurrent outside the depletion region for the ZnO and the CIGS, however, refers similarly to Eqs.(3.15) and (3.9). They become

$$J_p = \left[\frac{qF(1-R_i)\alpha_{ZnO}L_p}{\alpha_{ZnO}^2 L_p^2 - 1}\right] \times$$

$$\left\{ \frac{\left(\frac{S_p L_p}{D_p} + \alpha_{ZnO} L_p\right) - \exp(\alpha_{ZnO} x_j)\left[\frac{S_p L_p}{D_p}\cosh\left(\frac{x_j}{L_p}\right) + \sinh\left(\frac{x_j}{L_p}\right)\right]}{\frac{S_p L_p}{D_p}\sinh\left(\frac{x_j}{L_p}\right) + \cosh\left(\frac{x_j}{L_p}\right)} \right\}, \quad (4.3)$$

$$-\alpha_{ZnO} L_p \exp(-\alpha_{ZnO} x_j)$$

for excess minority holes in the ZnO and

$$J_n = \left[\frac{qF(1-R_i)\,\alpha_{CIGS}L_n}{\alpha_{CIGS}^2 L_n^2 - 1}\right] \exp\left(-\alpha_{CdS}W_{CdS} - \alpha_{ZnO}W_{ZnO} - \alpha_{CIGS}W_2\right) \times$$

$$\left\{ \frac{\left(\frac{S_n L_n}{D_n}\right)\left[\cosh\left(\frac{H'}{L_n}\right) - e^{-\alpha_{CIGS}H'}\right] + \sinh\left(\frac{H'}{L_n}\right) + \alpha_{CIGS}L_n e^{-\alpha_{CIGS}H'}}{\left(\frac{S_n L_n}{D_n}\right)\sinh\left(\frac{H'}{L_n}\right) + \cosh\left(\frac{H'}{L_n}\right)} - \alpha_{CIGS}L_n \right\}, \tag{4.4}$$

for excess minority electrons in the CIGS.

In case of $x_j > W_{ZnO}$, the n-region outside the depletion region covers entirely in ZnO and partially in CdS. The photocurrent in the p-region is the same as Eq.(4.4) and the photocurrent in the depletion region becomes

$$\begin{aligned} J_{dr} &= qF(1-R_i)\{\exp\left[-\alpha_{ZnO}W_{ZnO} - \alpha_{CdS}\left(x_j - W_{ZnO}\right)\right] \\ &\quad - \exp\left[-\alpha_{ZnO}W_{ZnO} - \alpha_{CdS}W_{CdS} - \alpha_{CIGS}W_2\right]\}. \end{aligned} \tag{4.5}$$

We use Eq.(4.3) as the current for excess holes in the n-region but $x_j$ is replaced by $W_{ZnO}$. In this work, it is easy to calculate the photocurrent, the conduction band spike of the CIGS-based solar cell in Fig.3.10 is not considered.

The total photocurrent is found by integrating the summation of photocurrent in each region over the wavelength,

$$J_L = \int_0^{\lambda_{max}} \left(J_p + J_{dr} + J_n\right)\, d\lambda. \tag{4.6}$$

This is shown in Fig.4.3, the photocurrent is not constant due to the variation of the depletion region on the applied voltage. We run the applied voltage from 0 V to 0.8 V because those values should cover the open circuit voltage. Spectral response of this current (see Fig.4.4) found at the short circuit shows that most photocurrent (see Fig.4.4) exists in the depletion region. The absorption coefficient of ZnO is less than that of CdS and CIGS, and is zero at the photon wavelength greater than 0.6 $\mu m$.

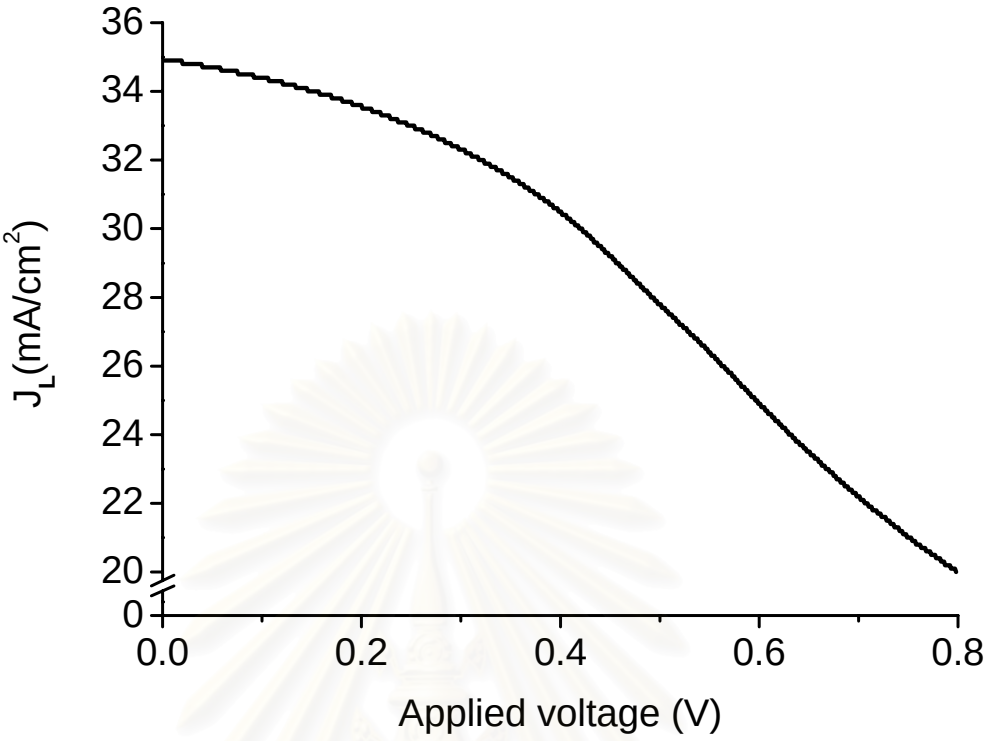


Figure 4.3: Calculated photocurrent of CIGS-based solar cells for various applied voltages.

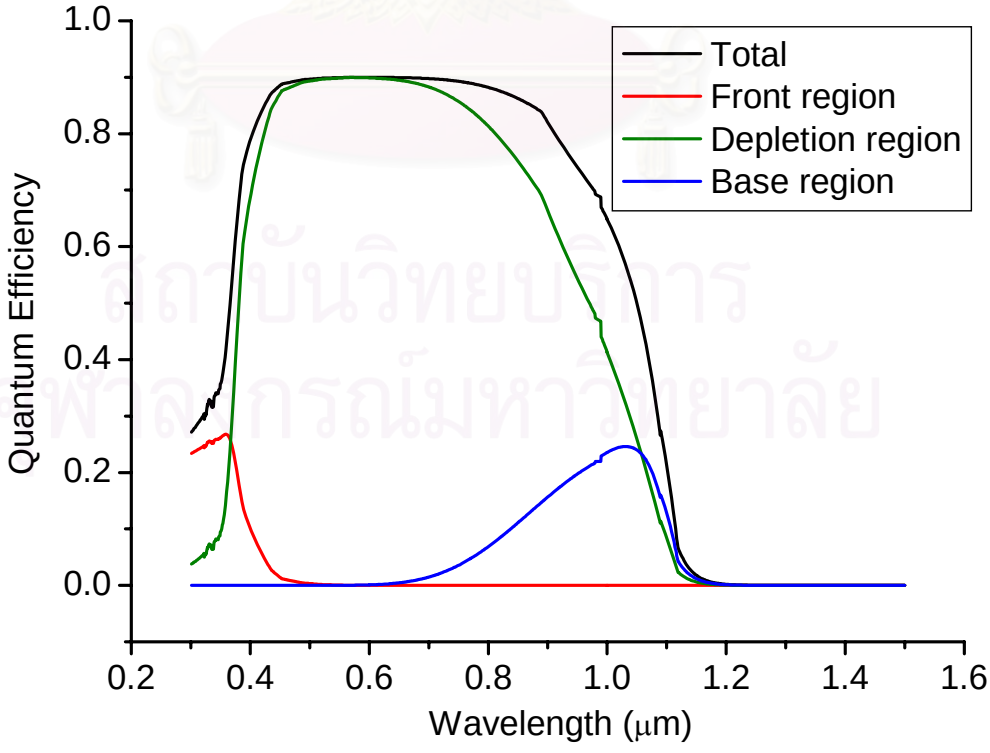


Figure 4.4: Computed quantum efficiency at the short circuit condition.

The absorption coefficient of CIGS is also high throughout the range of photon energy, which is less than 1.1 eV (about energy gap of CIGS), then photon flux remaining in the p-region is very low. These are reasons why the photocurrent in the depletion region is much greater than that in the p-region and in the n-region.

## 4.2 Circuit Model

A solar cell with an assumed grid pattern is modeled from the extensively adaptable use of the equivalent circuit of the solar cell as an interconnection of unit cells, namely a distributed network model. In this model, a two-dimensional path of current is used to emulate the transport of the current in the top layer material perpendicular to the grid. For example, Fig.4.5(a) shows the interconnection of unit cells for the solar cell with an assumed grid pattern. By considering the unit cells in the circle of Fig.4.5(a), the electrical circuits for the unit cells, which are exposed to light and in the dark (under the grid pattern), are shown in Fig.4.5(b). In the area with illumination, four halves of sheet resistance of the top layer of the solar cell ($\mathsf{R}$) are normalized by the number of unit cells and then confront at one end of them, namely a node. The node is connected to ground through the parallel connection of photocurrent, shunt resistance in the bulk of the solar cell and diode current, which is previously described in Chapter 3.

In the area without illumination, the electrical circuit is similar to that with illumination but the sheet resistance of the top layer of the solar cell is now replaced by that of the grid ($\mathsf{R_g}$) and normalized by the number of unit cells which the grid covers. Moreover, the term of photocurrent is not included since the grid blocks out the light reaching the solar cell. That is to say, the unit cell without illumination behaves like an ordinary diode. The unit cells with the covering grid are also taken at least one position to be the site of an applied voltage, a boundary voltage ($\mathsf{V_{bd}}$), according to the grid making contact with an external load

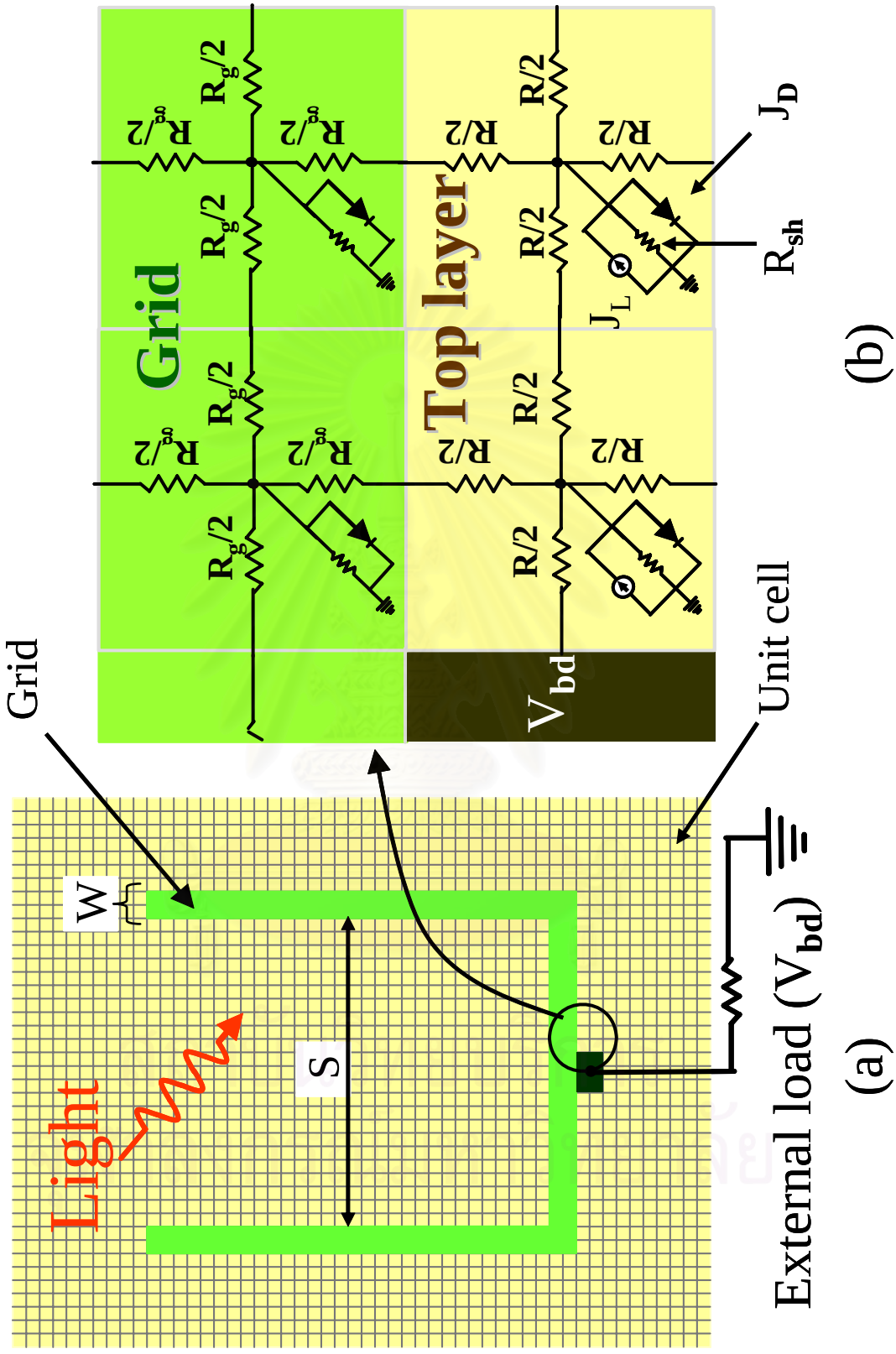


Figure 4.5: (a) Schematic diagram of the interconnection of unit cells for the solar cell with an assumed grid pattern. (b) The electrical circuits for the unit cells in the circle of Fig.4.5(a).

## 4.3 Evaluation Scheme

An assumed grid pattern is formed on the top of the solar cell. From the distributed network model, the solar cell is x unit cells wide and y unit cells long. For example, if x and y are 50 and 40, respectively, the entire solar cell has 2000 unit cells.

There are many parameters to know before setting an equation, which explains the circuit in each unit cell (see Fig.4.5), as follows. The shunt resistance of 10,000 Ω [8] in the bulk is sufficiently high that results may be only dominated by the series resistance in the solar cell. The resistance of the grid at the unit cell on which the grid covers is used in the form of sheet resistance, which should be much less than the sheet resistance of the top layer. Its value is assumed to be in the order of $1\times10^{-4}$ Ω/□. The sheet resistance of the top layer is the important parameter that impact the roll of the grid. We initially use the value of the sheet resistance of the top layer to be 10 Ω/□, which is as low as the value expected from the development of ZnO, the top layer. The photocurrent from the previous section has already been derived as well as the diode equation has been explained in section 3.8, Eqs.(3.30)-(3.32). The quality factor is about 1.52 according to Fig.3.11 at 300 K. Anyway, we use the data of $J_{sc}$ and $V_{oc}$ from Ref.(14) to find the reverse saturation current which is about $3.89\times10^{-9}$ A/cm$^2$. These related parameters must be used with Kirchhoff's current law to form a set of equations, illustrating the circuit model of the solar cell. For example, the equation representing the unit cell, which is exposed to light and connects to boundary voltage grids and the unit cell covered by grids, is given by

$$\frac{(V_{n,m}-V_{n,m+1})}{R}+\frac{(V_{n,m}-V_{n-1,m})}{R}+\frac{2\,(V_{n,m}-V_{n+1,m})}{R+R_g}+\frac{2\,(V_{n,m}-V_{bd})}{R}=$$
$$J_L-J_s\left[\exp\left(\frac{qV_{n,m}}{AkT}\right)-1\right]-\frac{V_{n,m}}{R_{sh}}, \tag{4.7}$$

where $V_{n,m}$ is the node voltage at point $(n,m)$, (row,column). The first two terms on the left hand side show the current related to the neighboring unit cells without

grids. The third and the forth terms on the left hand side are due to the unit cell with the grids and boundary voltage, respectively. By considering the group of no-grid-covering unit cells, the equation becomes

$$\frac{(V_{n,m}-V_{n,m+1})}{R}+\frac{(V_{n,m}-V_{n-1,m})}{R}+\frac{(V_{n,m}-V_{n,m-1})}{R}+\frac{(V_{n,m}-V_{n+1,m})}{R}= J_L-J_s\left[\exp\left(\frac{qV_{n,m}}{AkT}\right)-1\right]-\frac{V_{n,m}}{R_{sh}}. \quad (4.8)$$

There is no current term related to the boundary voltage since the unit cell does not connect to the boundary voltage grid. As well as the previous example, the equation of grid-covering unit cells becomes

$$\frac{(V_{n,m}-V_{n,m+1})}{R_g}+\frac{(V_{n,m}-V_{n-1,m})}{R_g}+\frac{(V_{n,m}-V_{n,m-1})}{R_g}+\frac{(V_{n,m}-V_{n+1,m})}{R_g}= -J_s\left[\exp\left(\frac{qV_{n,m}}{AkT}\right)-1\right]-\frac{V_{n,m}}{R_{sh}}. \quad (4.9)$$

From the above equation, the right hand side does not have the photocurrent term because of the grid blocking out the incident light. The diode current term on the right hand side of these equations is non-linear; therefore, we use Newton-Raphson method (see appendix A) to convert the equations to be a linear form. The system of linear equations is then solved by Gauss-Seidel iteration (see appendix B). The solution of the problem is a set of node voltages. In order to calculate the output current, the node voltages and the photocurrent are placed to the right hand side of the non-linear equation, which is summed up all unit cells;

$$J=\sum_n\sum_m\left\{J_L\delta_{n,m}-J_s\left[\exp\left(\frac{qV_{n,m}}{AkT}\right)-1\right]-\frac{V_{n,m}}{R_{sh}}\right\}, \quad (4.10)$$

where $\delta_{n,m}=1$ for the unit cell without the grid and $\delta_{n,m}=0$ for the unit cell with the grid. The process is repeated again for other boundary voltages from the short circuit to the open circuit. The J-V characteristics are made to carry out results, efficiency, fill factor, open circuit voltage, and short circuit current. Figure 4.6 summarizes all processes from the circuit model to analytical results.

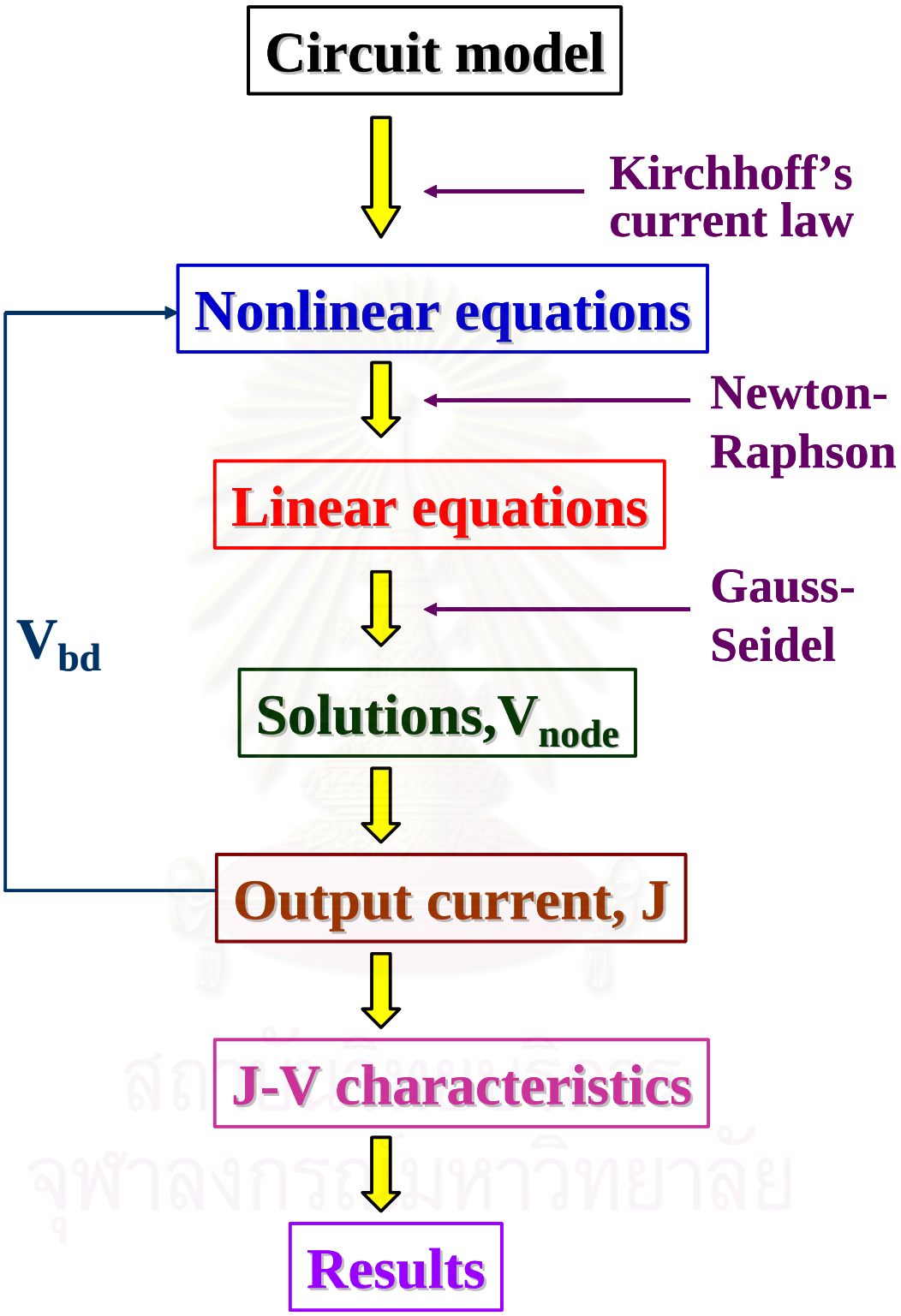


Figure 4.6: Flow diagram for the entire evalution scheme.

# CHAPTER 5

# Results and Discussions

In this chapter, results from the optimization are discussed. Firstly, we will describe node voltages, solutions for the system of equations, which are then used to find the output current at each boundary voltage. Secondly, the optimization used to estimate the relationship between the diffusion length and the width of the cell is shown. The optimization of fork-shaped grid patterns with two parallel arms determining grid parameters is shown in the third part. Lastly, the results of efficiency for the change of some layer properties are shown.

## 5.1 Node-Voltage Solutions

Node voltages are solutions of the system of non-linear equations obtained from a numerical method for such a solar cell with grid pattern in order to carry out the output current of each boundary voltage. The node voltages are monitored at a short circuit condition, for instance, using a square cell with each side of 10 unit cells wide and a point grid placed at the center of such the cell as shown in Fig.5.1. The profile of the node voltages is zero (dark) at the center, which is the position of the grid, and radially increases to the maximum (white) at the uttermost area. The electric field at the surface of the cell can be found from these surface potentials according to $\overrightarrow{\mathcal{E}} = -\overrightarrow{\nabla}\mathsf{V}$. It can be seen that the current created by the solar cell flows perpendicularly into the grid (see Fig.5.2). This result is due to the circuit model that the current is initially assumed to flow into the grid placed on the top layer of the solar cell.

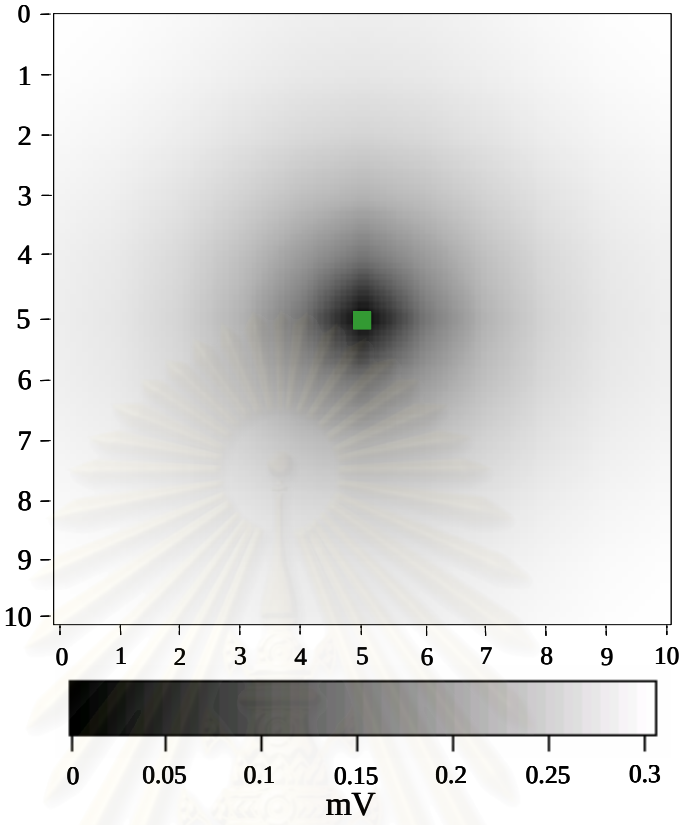


Figure 5.1: The profile of the node voltages for the cell with point grid at the center.

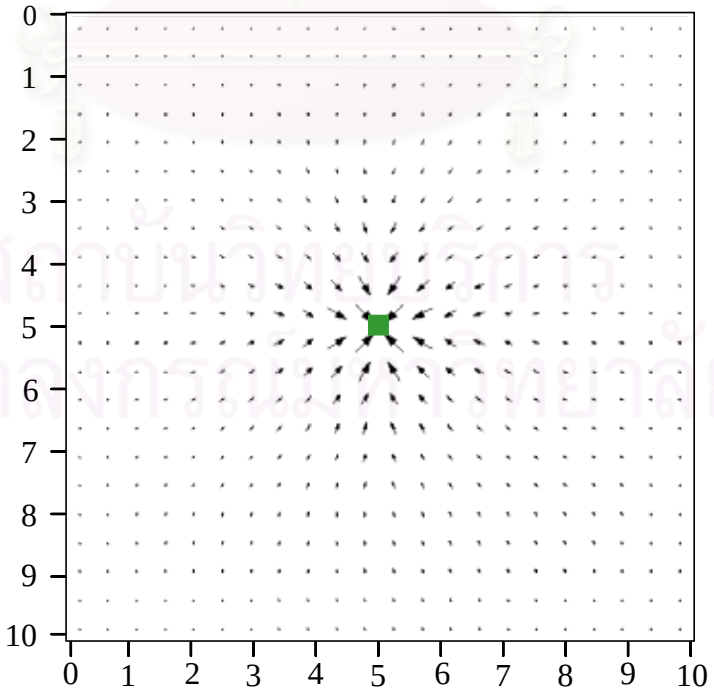


Figure 5.2: The direction of electric field at the surface of the cell. Arrows show the direction of the current flow into the position of the grid.

## 5.2 The Relationship between the Diffusion Length and the Width of the Cell

The purpose of this calculation is to study the influence of the diffusion length on the width of the cell. Because of the circuit model used here in this work, the diffusion length must be used in the form of the sheet resistance. The large value of the sheet resistance corresponds to the small value of the diffusion length. The solar cell used in this calculation is always 10 unit cell long, whereas the width $W_E$ of the cell is varied, as shown in Fig.5.3(a). The optimization uses a straight grid-line with one unit cell wide placing at the edge of the cell panel. The width $W_E$ of the cell varies from 3 to 30 unit cells. For long diffusion length (or small sheet resistance), carriers has higher chance to reach the grid, thus creating more current than that of low diffusion length. Therefore, the power loss of the current far from the grid is small.

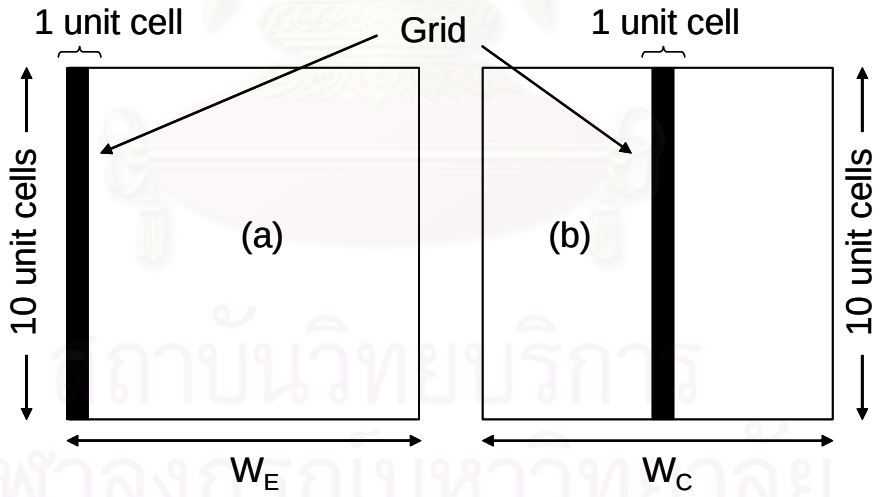


Figure 5.3: Schematic showing the straight grid-line placed at the edge (a) and at the center (b) on the top layer of the solar cell.

Figures 5.4 - 5.6 show the J-V characteristics for the sheet resistance of 10, 30 and 100 Ω/□. From these results, the increase of the exposed area for the sheet resistance of 10 Ω/□ influences highly to the increase of short circuit current. Unlike the short circuit current for the sheet resistance of 30 and 100 Ω/□, it rises

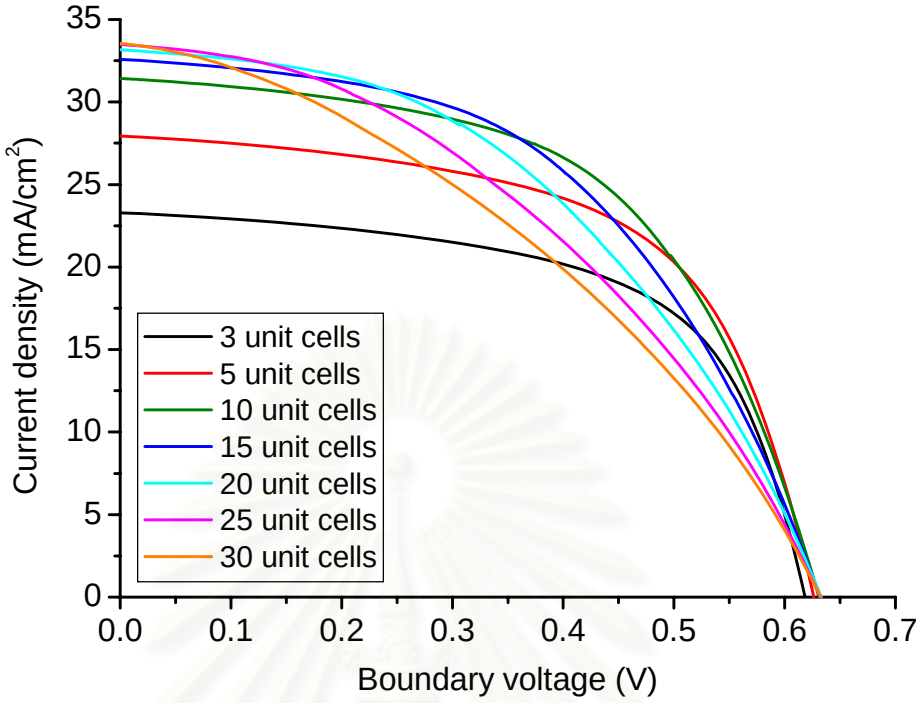


Figure 5.4: J-V characteristics of solar cells to estimate the relationship between the diffusion length and the width of the cell (under sheet resistance of 10 $\Omega/\square$).

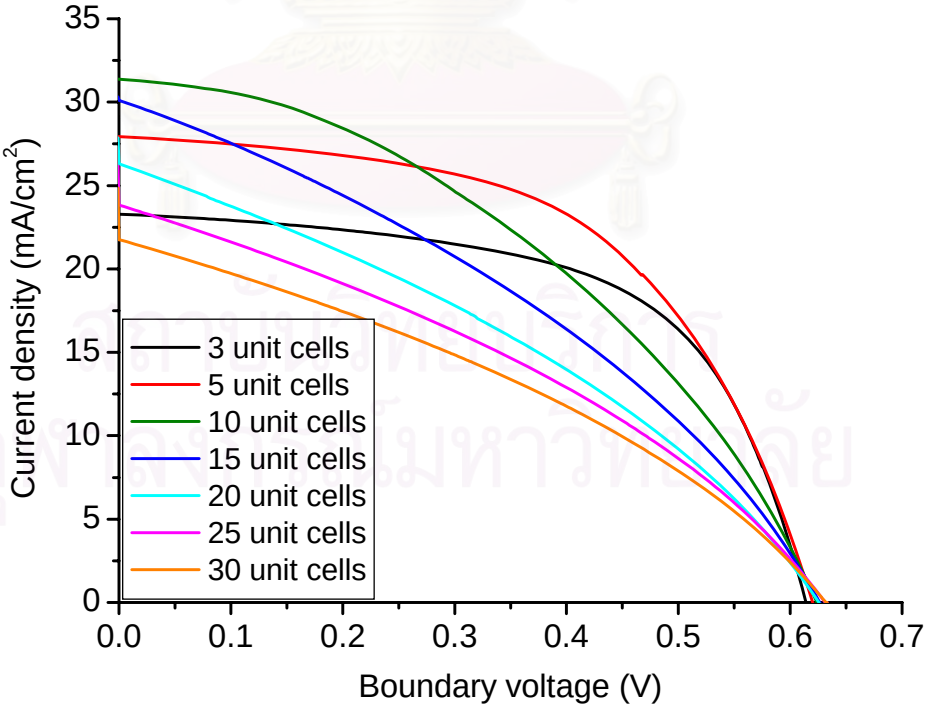


Figure 5.5: J-V characteristics of solar cells for estimating the relationship between the diffusion length and the width of the cell (under sheet resistance of 30 $\Omega/\square$).

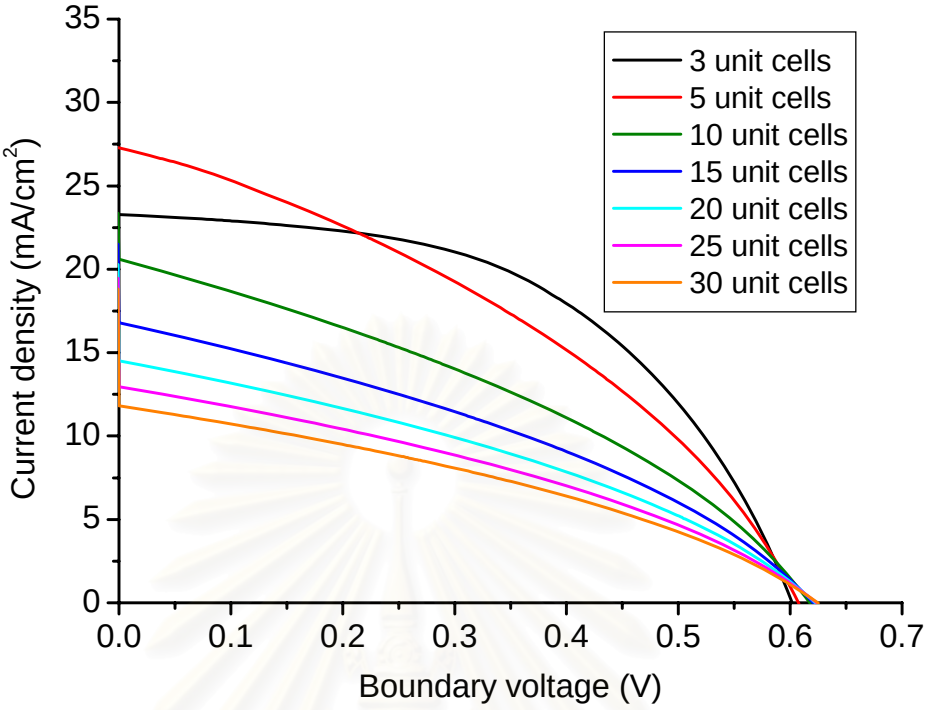


Figure 5.6: J-V characteristics of solar cells to estimate the relationship between the diffusion length and the width of the cell (under sheet resistance of 100 Ω/□).

to maximum by the effect of the exposed area and then lessens again due to the influence of resistance. Open circuit voltage changes a little for all used sheet resistances. Sheet resistance instead of shunt resistance causes the expansion of the open circuit voltage. The analysis on these J-V characteristics can be carried out and leads to the efficiency and the fill factor of the solar cell as described in Chapter 3.

At the same width of the cell, the efficiency of low sheet resistance is more than that of high sheet resistance as shown in Fig.5.7. The optimal width of the cell is about 10 and 5 unit cells for sheet resistance of 10 and 30 Ω/□, respectively. However, there is no optimal width for very high sheet resistance, 100 Ω/□. Due to the first two sheet resistances, the increase of the exposed area affects the rise of the efficiency. When $W_E$ is greater than the optimum width, the efficiency reduces again since the exposed area creates power less than the loss of power from the resistance that the current confront during the path of moving into grid. Anyway,

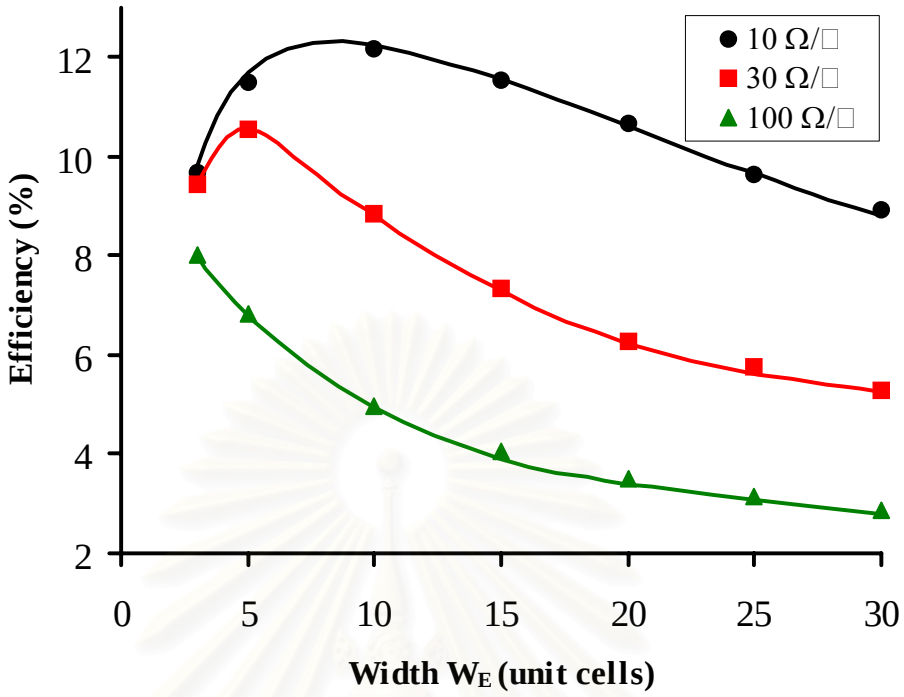


Figure 5.7: The efficiency extracted from the relationship between the diffusion length (or the sheet resistance) and the width $W_E$ of the cell. The optimization uses a straight grid-line placed at the edge of the cell panel.

the decrease of the efficiency for sheet resistance of 100 Ω/□ is mainly caused by the effect of the resistance, although exposed area still build up the power.

Fill factor of the above optimization is shown in Fig.5.8. The fill factor decreases linearly as the width of sheet resistance of 10 Ω/□ increases, but very rapidly for the remainings and more or less saturates beyond the width of 10 unit cells.

If the position of the used grid is changed to the center of the cell panel (see Fig.5.3(b)) with the width $W_C$ varying from 5 to 35 unit cells, the optimal width of the cell can be found for the sheet resistance of 10 and 30 Ω/□ at 19 and 9 unit cells, respectively, as shown in Fig.5.9. As well as the first case, the optimization cannot be obtained with the sheet resistance of 100 Ω/□. The trend of change of the efficiency is quite similar to that of the grid placing at the edge, but the change is at lower rate. Because of this, the placement of the grid at the center compared with at the other one is equivalent to reducing the path that current flow into the

grid in the same distance.

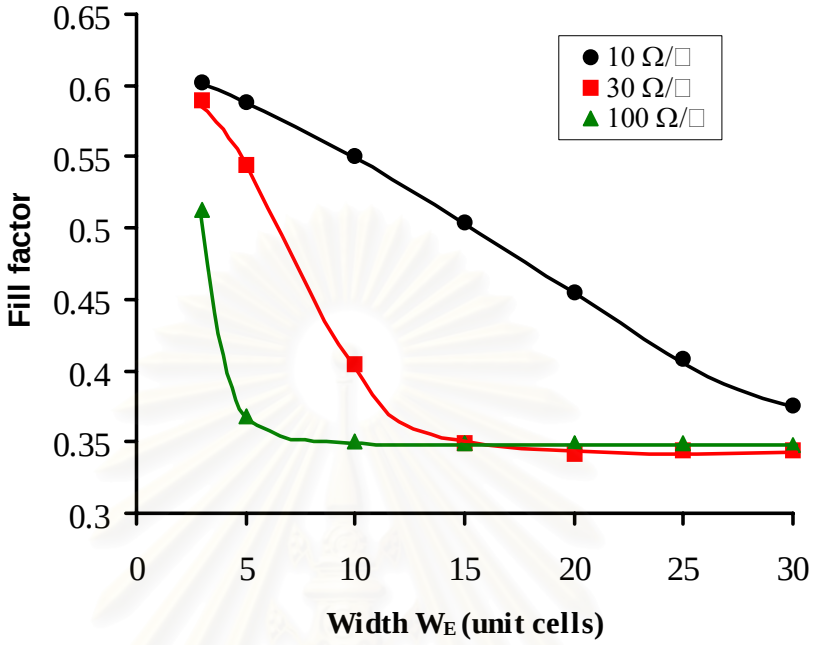


Figure 5.8: The fill factor extracted from the relationship between diffusion length (or sheet resistance) and the width $W_E$ of the cell.

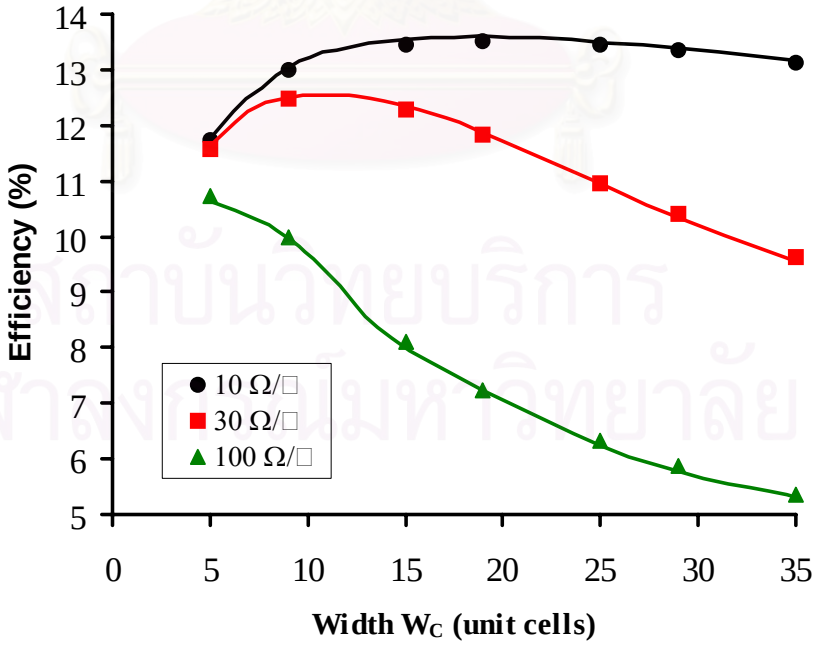


Figure 5.9: The efficiency extracted from the relationship between the diffusion length and the width $W_C$ of the cell. The optimization uses the straight grid-line placed at the center of the cell panel.

## 5.3 The Optimization for Fork-Shaped Grid Patterns

The fork-shaped grid pattern is expected to be the effective pattern [30] because it is similar to the comb-shaped grid used in the large area of the silicon based solar cell [31], but the the fork-shaped grid has only one bus bar and two arms. Hence, the study focuses on parameters of the pattern, e.g. the spacing S between the two arms and the width W of each arm. All two types of doubt were performed on the top of the square solar cell divided into 2500 unit cells, each side of 50 unit cells. The two arms are also parallel to each other and connected by a bus bar, as shown in Fig.5.10.

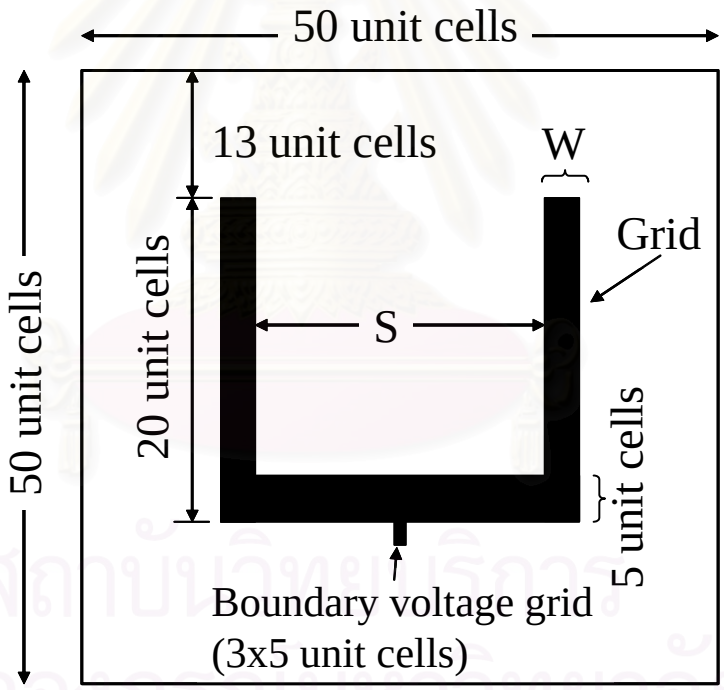


Figure 5.10: Schematic showing the fork-shaped grid on the top layer of the solar cell.

In order to estimate the first parameter, the optimization uses the arms which are one unit cell wide and 20 unit cells long. The top of the arm is 13 unit cells far from the side of the panel. The bus bar used to collect current from the arms is 5 unit cells wide. The length of the bus bar varies with the variation of the spacing S. The unit cells of the boundary voltage are placed at the bottom of the

bus bar. The spacing is taken to be 4, 10, 14, 20, 24, 30 and 34 unit cells to find the optimal one associated with the sheet resistance of 10, 30, 50, 70 and 100 Ω/□. For such the variation, the J-V characteristics are shown in Figs.5.11 - 5.15. These results show that the short circuit current increases when the spacing decreases. The increase of the spacing causes the expansion of the bus bar length, whereas its width is still constant. As a result, the area exposed to light decreases. Figure 5.16 shows the J-V characteristics, in which the spacing S of 4 unit cells, for each sheet resistance plotted together. At the same boundary voltage, the output current increases with the decrease of the sheet resistance. This is because the resistance causes the obstruction to the current in the circuit, according to Ohm's law. In addition, the open circuit voltage does not change because the shunt resistance used in the circuit model is sufficiently high and always fixed at the same value.

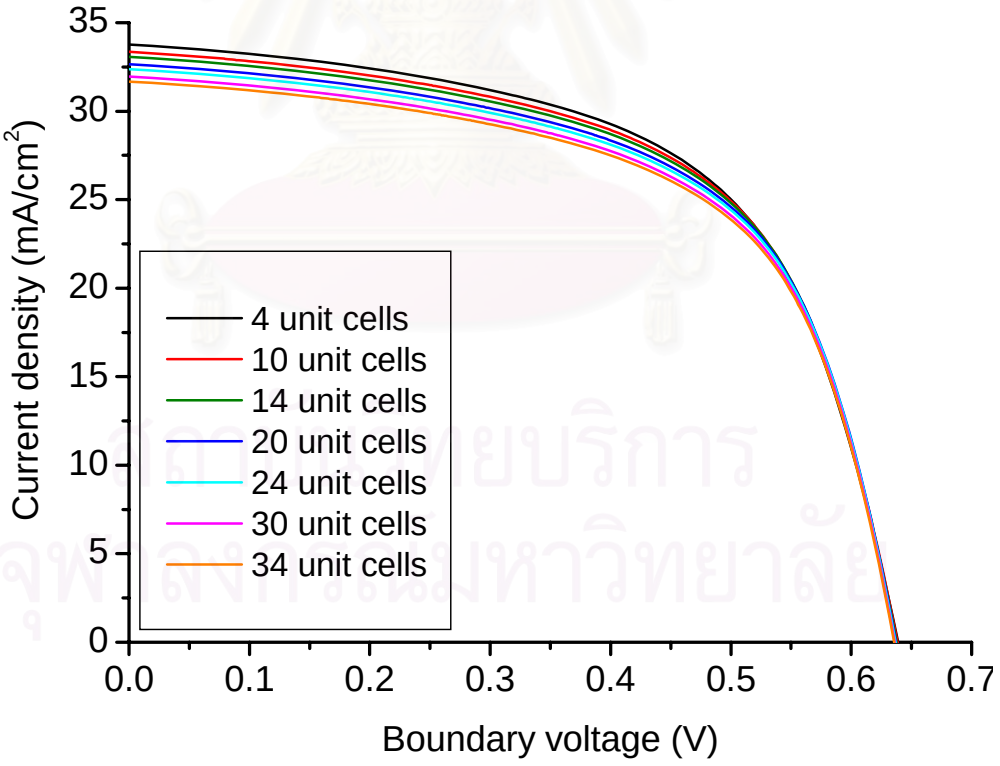


Figure 5.11: J-V characteristics of solar cells with the sheet resistance of 10 Ω/□.

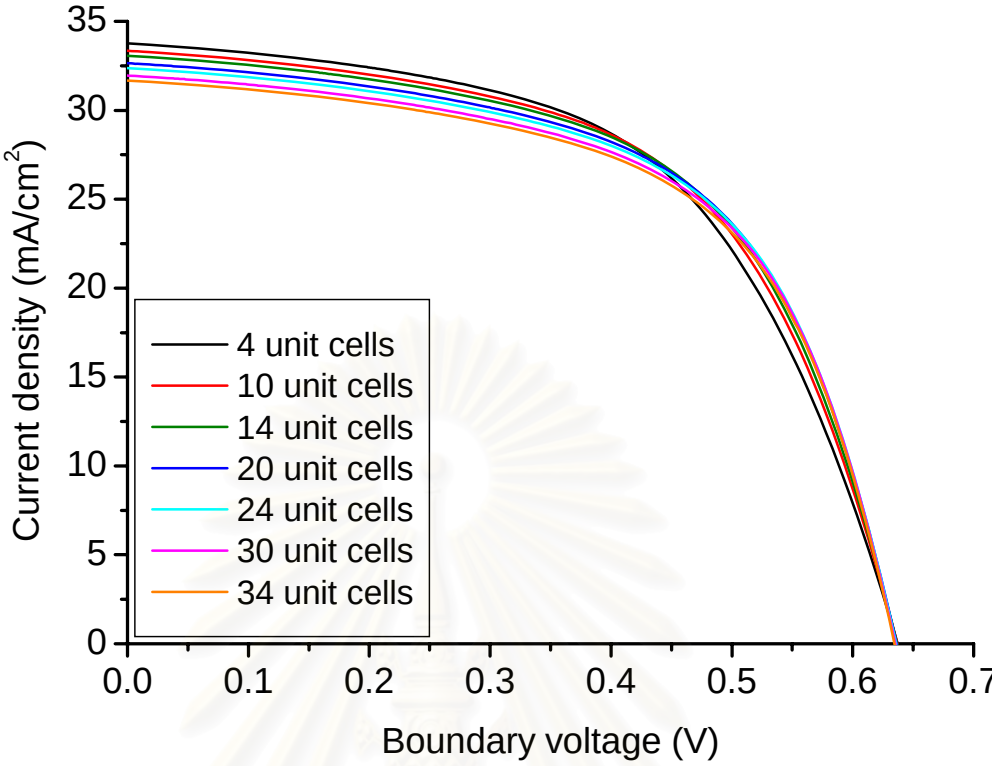


Figure 5.12: J-V characteristics of solar cells with the sheet resistance of 30 Ω/□.

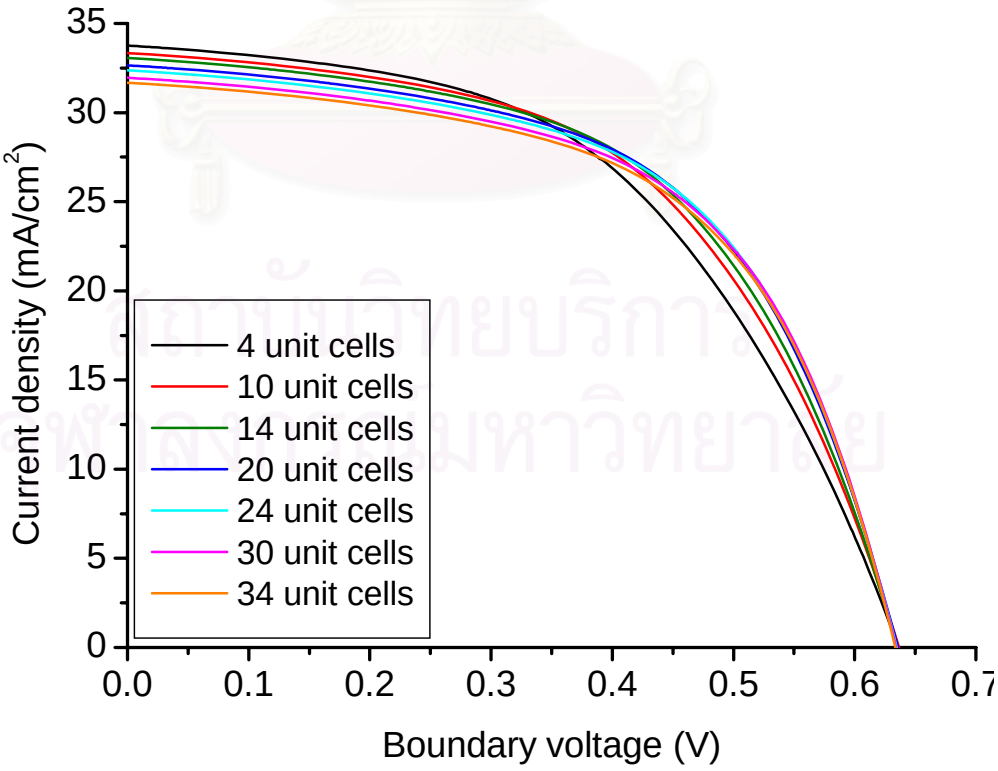


Figure 5.13: J-V characteristics of solar cells with the sheet resistance of 50 Ω/□.

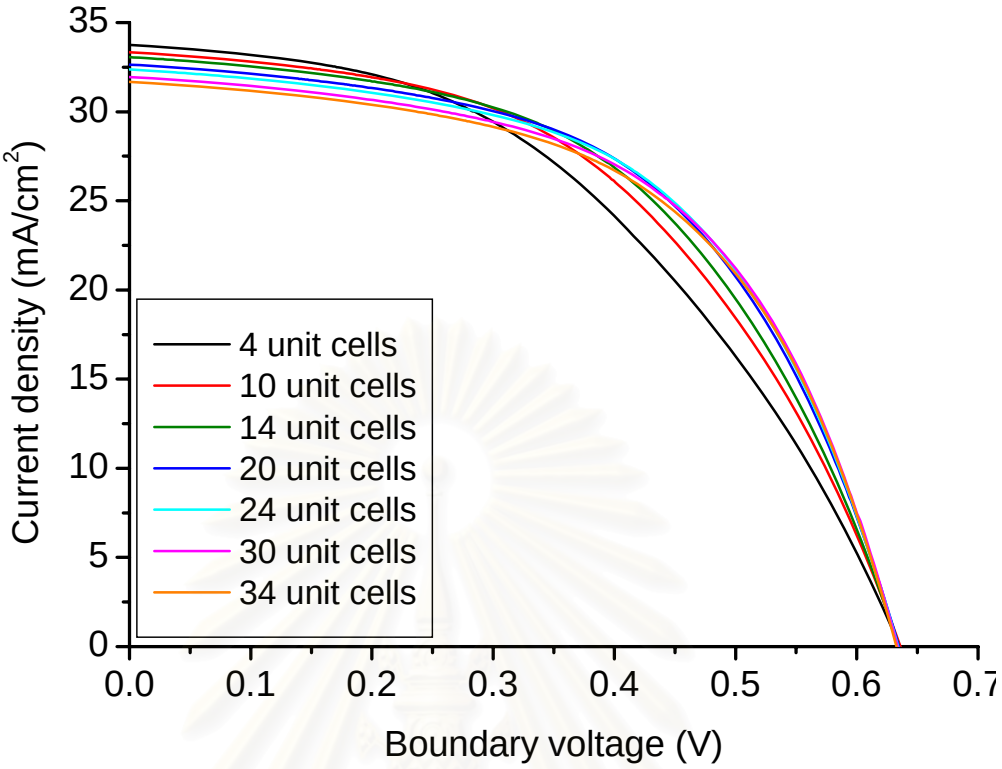


Figure 5.14: J-V characteristics of solar cells with the sheet resistance of 70 Ω/□.

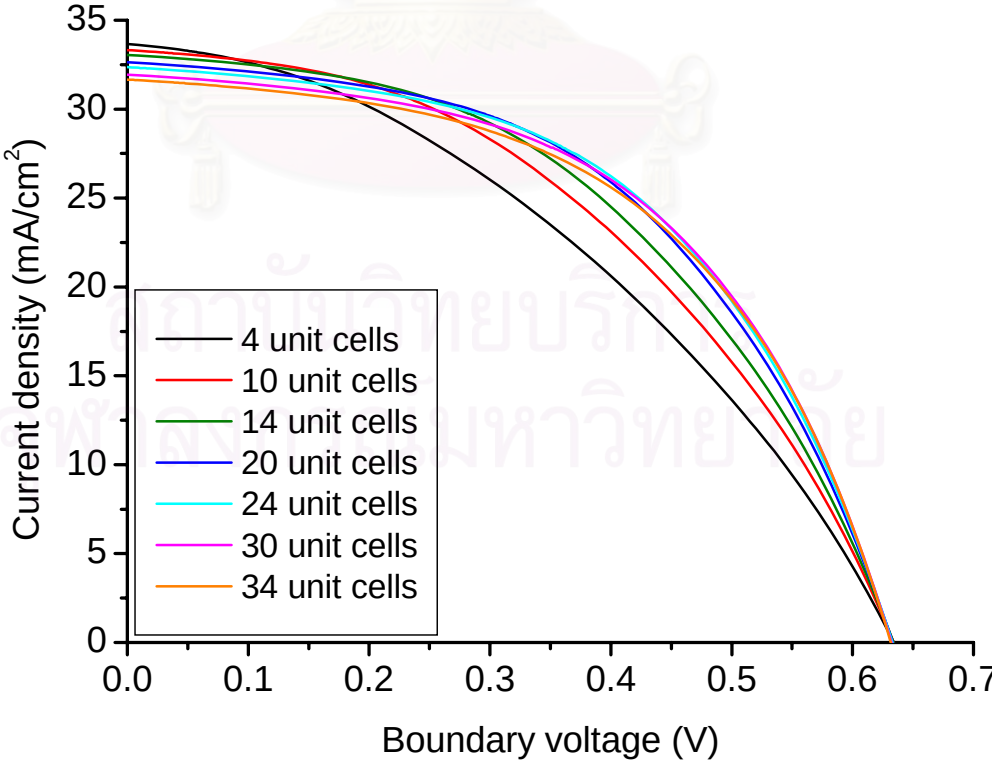


Figure 5.15: J-V characteristics of solar cells with the sheet resistance of 100 Ω/□.

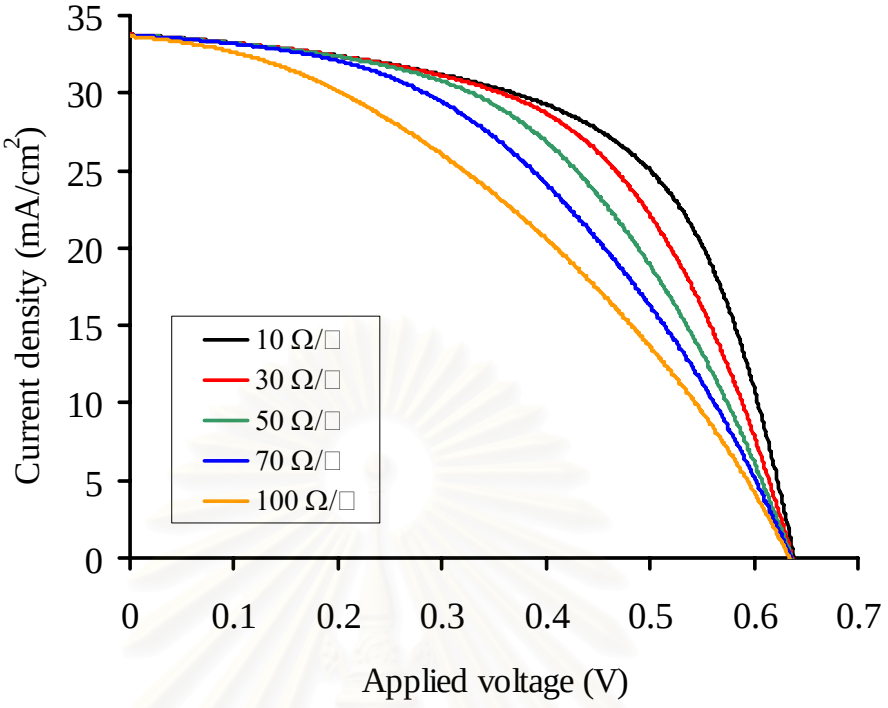


Figure 5.16: Selected plot of J-V characteristics of solar cells at the spacing of 4 unit cells.

The effect of varying the spacing S on the efficiency is shown in Fig.5.17 for various sheet resistances. For the same spacing, it has been seen that the larger the sheet resistance, the smaller the efficiency is obtained. It can be explained that for larger sheet resistance or shorter diffusion length, the carriers cannot reach the grid before the recombination processes occur, thus lowering the output current collected by the grid as shown in Fig.5.16. Therefore, the maximum power decreases when the sheet resistance increases. In the case of a sheet resistance of 10 Ω/□, the efficiency decreases monotonicly as the spacing S increses. In other words, there is no optimization for this case. This value of sheet resistance is so small to find the optimal one of the spacing then the effect of shaded area via the expansion of the bus bar is more effective than that of the resistance. Furthermore, for the sheet resistance greater than 10 Ω/□, the optimal spacing takes place at different values. An increase in the optimum is an increase in the value of sheet resistance. The curves of low sheet resistances do not change drastically as that

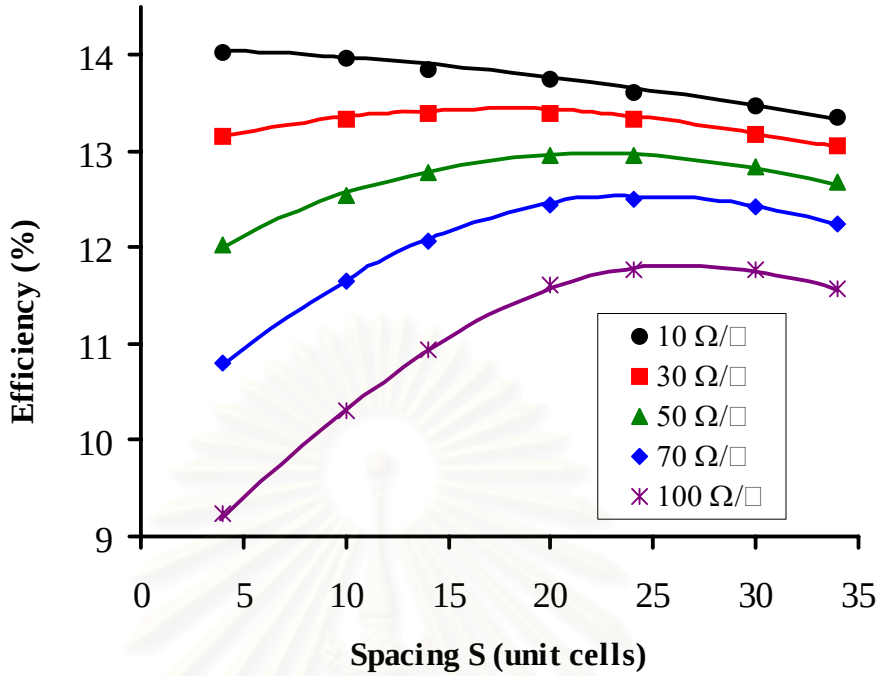


Figure 5.17: The efficiency as a function of the spacing S between the two arms of fork-shaped grid for various sheet resistances.

of larger sheet resistances since the shaded area still affects the efficiency but less than the sheet resistance does. It can be expected that the optimum is easy to observe when the sheet resistance is large enough. Besides, the optimal spacing is about 17, 21, 24 and 26 unit cells for the sheet resistance of 10, 30, 50 and 100 Ω/□, respectively.

Figure 5.18 illustrates the fill factor as a function of the spacing S of various sheet resistances. The fill factor increases rapidly as spacing increases, then decreases again after the maximal one. It is obviously observed in the larger value of sheet resistance.

Similar to the estimation of the appropriate spacing, the width W of the arms is optimized to attain the best efficiency for the best one. The optimization uses the sheet resistance and the detail of the fork-shaped grid similar to the first case but the width W of the arms varies form 1 to 5 unit cells. The spacing S between the two arms is also always fixed at 34 unit cells throughout this optimization.

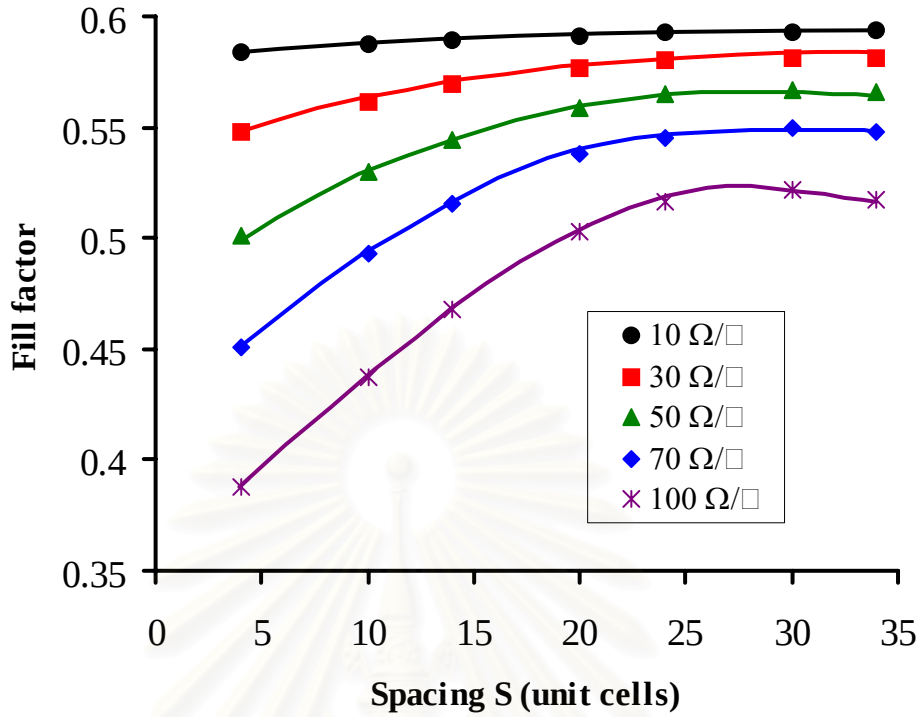


Figure 5.18: The fill factor as a function of the spacing S between the two arms of fork-shaped grid for various sheet resistances.

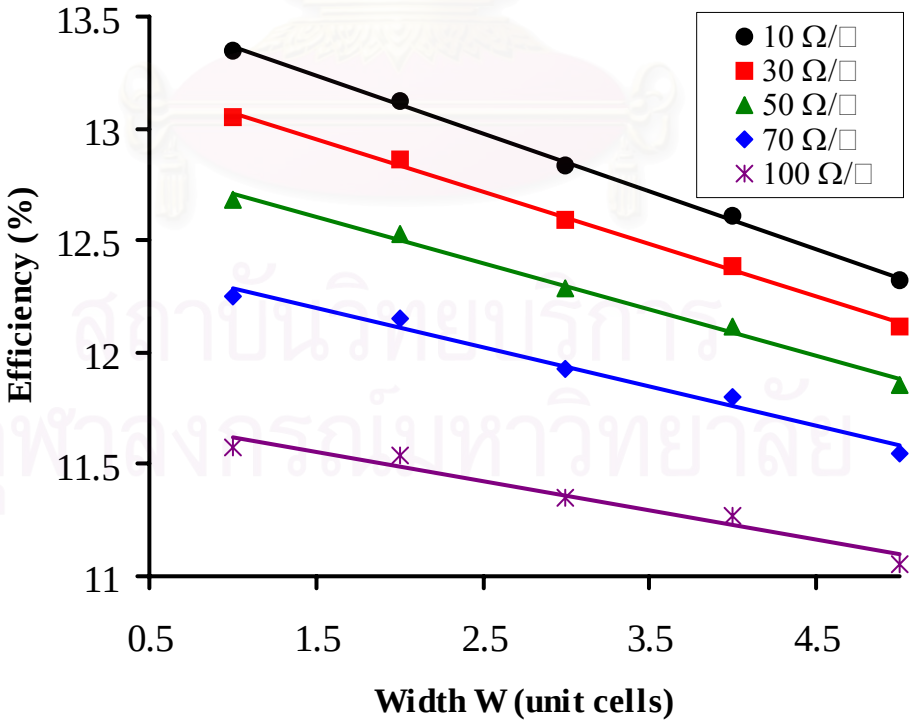


Figure 5.19: The efficiency as a function of the width W of the arms when the spacing is alway fixed at 34 unit cells for various sheet resistances.

The spacing of 34 unit cells is the value that the width of each arm with one unit cell wide passes the maximal efficiency or has been already optimized for the appropriate one, so that the optimization of the width of the arms is performed to recover the efficiency. Figure 5.19 shows the efficiency affected by the change of the width W of each arm, indicating that there are no optimal widths. The increase of the width degrades the efficiency. It is so that the optimization is not successful since the increase of shaded area has stronger impact than the decrease of the resistance when the width expands.

## 5.4 Results on the Change of Layer Property

The CIGS-based thin film solar cells with different elemental composition are measured for the efficiency at the normally experimental properties of each layer, i.e., ZnO, CdS and CIGS as described in Chapter 4. We also use the details of the solar cell with grid pattern as in Section 5.1. Consequently, the efficiency is achieved at 13.42% for the sheet resistance of 10 $\Omega/\square$. The efficiencies with the change of some layer properties are summarized in Table 5.1.

Table 5.1: The efficiency affected by the change of layer property in such the solar cell.

| The change of layer property | Before | | After | |
|---|---|---|---|---|
| | | $\eta$ (%) | | $\eta$ (%) |
| Sheet resistance | 10 $\Omega/\square$ | 13.42 | 1 $\Omega/\square$ | 14.68 |
| | | | 0.1 $\Omega/\square$ | 14.79 |
| Reflectivity | 10% | | 0% | 14.79 |
| Absorption coef. of ZnO | $\alpha_{ZnO}$ | | $\alpha_{ZnO}/100$ | 13.59 |
| Absorption coef. of CIGS | $\alpha_{CIGS}$ | | $\alpha_{CIGS}/100$ | 2.31 |
| Diffusion coef. of electron in ZnO | $D_p$ | | $D_p \times 100$ | 13.45 |
| Diffusion coef. of electron in CIGS | $D_n$ | | $D_n \times 100$ | 14.17 |

The reflectivity of 0% refers to the photon entering the cell cannot reflect back out of the cell. Thus it generates electron-hole pairs with no less. The change of absorption coefficient concerns with the photon flux which creates the electron-hole pairs. Most of photons absorbed by ZnO make the electron-hole pairs

far from the junction edge compared with the diffusion length of excess minority carrier in ZnO. Then, the decrease of the absorption coefficient of ZnO causes the increase of the remaining photon flux in SCR and the p-region. However, the decrease of absorption coefficient of CIGS degrades the efficiency rapidly because almost photon flux is absorbed in CIGS. Finally, the increase of diffusion coefficient effects the improvement of the diffusion length, therefore raising the efficiency.

# CHAPTER 6

# Conclusions

The optimization provides the understanding of the grid designs used in solar cells and a way to optimize them. The procedure of the optimization is to calculate the photo-generated current in the bulk of the solar cell based on the structure Cu(In,Ga)$Se_2$/CdS/ZnO/metal-grid. We use the experimental properties of each layer in such structure. The photo-generated current is in the range less than 35 $mA/cm^2$ and varies as a function of an applied voltage because the space charge region (SCR) width in the junction always changes with the variation of the applied voltage. That is to say, the photo-generated current decreases as the applied voltage increases. The change of the layer properties such as absorption coefficient, reflectivity and diffusion coefficient (later affecting the diffusion length) can raise or lessen the amount of the photo-generated current, thus changing the efficiency of the cell. The efficiency of the cell with normal layer properties can be found at about 13%-14%. From the spectral response, the electron-hole pairs in the SCR mainly cause the photo-generated current.

In this work, the optimization is based on the use of distributed network model and Kirchoff's current law to form a system of non-linear equations that describes the solar cell with grid pattern. They are solved by a numerical method to carry out the node voltages of each unit cell in the entire solar cell. An output current at each boundary voltage is then calculated from these node voltages. We use the JV-characteristics to find cell parameters, especially the efficiency. The profile of node voltages (or surface potentials) shows that the current at surface of the cell flows perpendicularly to the grid edge. The current runs toward the grid

because the grid is assumed on the positive side of the cell.

From the result of the relationship between the diffusion length and the width of the cell using the straight grid-line placed at the edge of the cell, it is found that the optimal width of the cell depend on the diffusion length as expected. The optimal width of high diffusion length is more than that of low diffusion length. However, it does not occur for very low diffusion length. For the sheet resistance of 10 $\Omega/\square$, the optimal width is about 10 unit cells when the straight grid-line is placed at the edge of the cell panel. This means that if the solar cell is 100 unit cells wide, we must use 5 straight grid-lines laid on the solar cell to collect the current from the cell that the distance between each line is 20 unit cells.

The results from the use of the fork-shaped grid with two parallel arms show that the optimal spacing between the two arms can be obtained for most of used sheet resistances. This optimum depends on the loss of efficiency due to shaded area and resistance. For higher sheet resistance or shorter diffusion length, the spacings between the arms get larger. This shows that the optimal spacing plays much more role to collect carriers far from the grid before the recombination takes place. On the other hand, the optimal width of each arm cannot be deduced from any use of sheet resistance because the increase of shaded area has stronger impact than the decrease of the resistance when the width expands.

For consideration of the effect of sheet resistance on the efficiency, the loss of the efficiency is also caused by the increase of the sheet resistance at the same condition. As a result, the front layer of the cell must have small value of sheet resistance. In addition, analysis of all JV-characteristics shows that the open circuit voltage is rather constant at about 0.64 V. The short circuit current depends on the amount of the area exposed to light. It also concerns with the diffusion length. Lastly, the fill factor cannot be concluded in the same way since the change of the fill factor depends on other three parameters, efficiency (or maximum output power), short circuit current and open circuit voltage.

# REFERENCES


1. Green, M.A. Solar Cells: Operating principles, technology, and system applications. New Jersey: Prentice-Hall, 1982.

2. Sharma, B.L. and Purohit, R.K. Semiconductor Heterojunctions. vol.5. Oxford: Pergamon Press, 1974.

3. Green, M.A. and et.al. Solar cell efficiency tables (version 22): Progress in Photovoltaics: Research and Applications. 11(2003): 347-352.

4. Contreras, M.A. and et.al. Progress Toward 20% Efficiency in Cu(In,Ga)$Se_2$ Polycrystalline Thin-film Solar Cells. Progress in Photovoltaics: Research and Applications. (1999).

5. Kessararat Ugsornrat. Transparent conducting ZnO(Al) thin films deposited by sequential RF and DC magnetron sputtering. Master's Thesis, Department of Physics, Faculty of Science, Chulalongkorn University, 2002.

6. Zhao, J., Wang, A., Abbaspour-Sari, E., Yun, F. and Green, M.A. Improved efficiency silicon solar cell module. IEEE Electron Device Letters. 18(2) (1997): 48-50.

7. Antonini, A. and et. al. Contact grid optimization methodology for front contact concentration solar cells. Solar Energy Mater. Sol. Cells 80 (2003): 155-166.

8. Annamalai, N.K., Blanchard, R.F. and Bockman, J.F. A numerical method to opimize collector grids. IEEE (1989): 205-210.

9. Neamen, D.A. Semiconductor Physics & Devices: Basic Principles. 2nd ed. Chicago: McGraw-Hill, 1997.

10. Cooke, M.J. Semiconductor Devices. New York: Prentice-Hall, 1990.

11. Sze, S.M. Physics of Semiconductor Devices. 2nd ed. New York: John Wiley & Sons, 1981.

12. Milnes, A.G. and Feucht, D.L. Heterojunctions and Metal-Semiconductor Junctions. New York: Academic Press, 1972.

13. Panita Chinvetkitvanich. Electrical Characterization of ZnO/CdS/Cu(In,Ga)$Se_2$ Thin Film Solar Cells. Master's Thesis, Department of Physics, Faculty of Science, Chulalongkorn University, 2001.

14. Hovel, H.J. Semiconductors and Semimetals. vol.11. New York: Academic Press, 1975.

15. Standard Tables for Reference Solar Spectral Irradiance at Air Mass 1.5: Direct normal and hemispherical for a 37 degree titled surface, Available from: http://rredc.nrel.gov/solar/spectra/am1.5/ (1999, June).

16. Stuckings, M.F. and Blakers, A.W. A study of shading and resistive loss from the fingers of encapsulated solar cells. Solar Energy Mater. Sol. Cells 59(1999): 233-242.

17. Contreras, M.A., and et.al. Properties of 19.2% Efficiency ZnO/CdS/$CuInGaSe_2$ Thin-film Solar Cells. Progress in Photovoltaics 11 (2003): 1-6.

18. Kessler, J., Bodegård, M., Hedström, J. and Stolt, L. New world record Cu(In,Ga)$Se_2$ based mini-module: 16.6%. In Preceedings 16th European Photovoltaic Solar Energy Conference (2000): 2057-2060.

19. Rau, U. and Schock, H.W. Electronic properties of Cu(In,Ga)$Se_2$ heterojunction solar cells-recent achievements, current understanding, and future challenges. Appl. Phys. A. 69 (1999): 131-147.

20. Rau, U., Jasenek, A., Schock, H.W., Engelhardt, F. and Meyer, Th. Electronic loss mechanisms in chalcopyrite based heterojunction solar cells. Thin Solid Films 361-362 (2000): 298-302.

21. Nadenau, V., Rau, U., Jasenek, A. and Schock, H.W. Electronic properties of $CuGaSe_2$-based heterojunction solar cells Part I. Transport analysis. J. Appl. Phys. 87(1) (2000): 584-593.

22. Rau, U. Tunneling-enhanced recombination in Cu(In,Ga)$Se_2$ heterojunction solar cells. Appl. Phys. Lett. 74(1) (1999): 111-113.

23. Hou, J. and Fonash, S.J. An experimental and computer simulation study of the role of CdS in CIS-type solar cells. IEEE 25th PVSC (1996): 961-964.

24. Topič. M., Smole, F. and Furlan, J. Examination of blocking current-voltage behaviour through defect chalcopyrite layer in ZnO/CdS/$CuInGaSe_2$/Mo solar cell.Solar Energy Mater. Sol. Cells 49 (1997): 311-317.

25. Köntges, M. and et. al. Light induced changes in the electrical behavior of CdTe and Cu(In,Ga)$Se_2$ solar cells. Thin Solid Films 403-404 (2002): 280-286.

26. Agostinelli, G., Bätzner, D.L. and Burgelman, M. A theoretical model for the front region of cadmium telluride solar cells. Thin Solid Films 431-432 (2003): 407-413.

27. Agostinelli, G. and et. al. Light dependent current transport mechanism in chalcogenide solar cells. 3rd WCPEC, Osaka, Japan (2003)

28. Markus Gloeckler. Numerical Modeling of CIGS Solar Cells: Definition of the baseline and explanation of superposition failure. Master's Thesis, Department of Physics, Colorado State University, 2002.

29. Gloeckler, M., Fahrenbruch, A.L. and Sites, J.R. Numerical Modeling of CIGS and CdTe Solar Cells: Setting the Baseline. The World Conf. on Photovoltaic Energy Conversion, Tokyo, Japan, 2003.

30. Wennerberg, J., Kessler, J. and Stolt, L. Cu(In,Ga)$Se_2$-based thin-film photovoltaic modules optimized for long-term performance. Solar Energy Mater. Sol. Cells 75 (2003): 47-55.

31. Zhao, J., Wang, A., Abbaaspour-Sani, E., Yun, F. and Green, M.A. Improved Efficiency Silicon Solar Cell Module. IEEE Electron Device Letters 18(2) (1997): 48-50.

# APPENDICES

# APPENDIX A

# Newton-Raphson Method

There are many problems that we cannot use an ordinary iteration to solve because they are not linear equations. The Newton-Raphson method can be used to find roots for this kind of problem.

For an example, we start with a pair of equations involving two variables $x_1$ and $x_2$;

$$\begin{cases} f_1(x_1, x_2) = 0 \\ f_2(x_1, x_2) = 0 \end{cases}. \tag{A.1}$$

Suppose, we take $(x_1, x_2)$ as an approximate solution of Eq.(A.1). With the corrections $h_1$ and $h_2$, $(x_1 + h_1, x_2 + h_2)$ will be a better approximate solution. We then expand both functions to the first order of Taylor's series;

$$\begin{cases} 0 = f_1(x_1 + h_1, x_2 + h_2) \approx f_1(x_1, x_2) + h_1 \frac{\partial f_1}{\partial x_1} + h_2 \frac{\partial f_1}{\partial x_2} \\ 0 = f_2(x_1 + h_1, x_2 + h_2) \approx f_2(x_1, x_2) + h_1 \frac{\partial f_2}{\partial x_1} + h_2 \frac{\partial f2}{\partial x_2} \end{cases}. \tag{A.2}$$

The partial derivatives in Eq.(A.2) is evaluated at $(x_1, x_2)$. Therefore, equation (A.2) becomes a pair of linear equations for determining $h_1$ and $h_2$. The coefficient matrix is the Jacobian matrix of $f_1$ and $f_2$;

$$J = \begin{bmatrix} \frac{\partial f_1}{\partial x_1} & \frac{\partial f_1}{\partial x_2} \\ \frac{\partial f_2}{\partial x_1} & \frac{\partial f2}{\partial x_2} \end{bmatrix}. \tag{A.3}$$

We can reorganize Eq.(A.2) as a matrix-vector form;

$$-\begin{bmatrix} f_1(x_1^k, x_2^k) \\ f_2(x_1^k, x_2^k) \end{bmatrix} = J \begin{bmatrix} h_1^k \\ h_2^k \end{bmatrix}. \tag{A.4}$$

If the Jacobian matrix is nonsingular, we obtain the solution by using the iteration as for a linear system. The solution is

$$\begin{bmatrix} h_1^k \\ h_2^k \end{bmatrix} = -J^{-1} \begin{bmatrix} f_1(x_1^k, x_2^k) \\ f_2(x_1^k, x_2^k) \end{bmatrix}. \tag{A.5}$$

Then, the new estimated solution for two nonlinear equations is

$$\begin{bmatrix} x_1^{k+1} \\ x_2^{k+1} \end{bmatrix} = \begin{bmatrix} x_1^{k} \\ x_2^{k} \end{bmatrix} + \begin{bmatrix} h_1^{k} \\ h_2^{k} \end{bmatrix}, \tag{A.6}$$

where $k$ and $k+1$ are the present and future computation, respectively.

# APPENDIX B

# Gauss-Seidel Iteration

Gauss-Seidel is one of the iterative or approximate methods, which is used to obtain roots for a system of equations. The iteration consists of guessing a value and using a systematic method to obtain a refined estimate of the roots. Assume that we have a set of linear equations;

$$[A]\{X\} = \{B\}. \tag{B.1}$$

For an example, we will solve a 3×3 set of equation. If the diagonal are all nonzero, the first equation can be solved to yield for $x_1$, the second for $x_2$, and the third for $x_3$;

$$x_1 = \frac{b_1 - a_{12}x_2 - a_{13}x_3}{a_{11}} \tag{B.2}$$

$$x_2 = \frac{b_2 - a_{21}x_1 - a_{23}x_3}{a_{22}} \tag{B.3}$$

$$x_3 = \frac{b_3 - a_{31}x_1 - a_{32}x_2}{a_{33}}. \tag{B.4}$$

The solution can be solved by choosing guesses for the x's. The initial guesses are substituted into Eq.(B.2) to calculate a new value of $x_1$. Then, we use this new value of $x_1$ along with the previous guess of $x_3$ for Eq.(B.3) to compute a new value of $x_2$. The calculation is reported for Eq.(B.4) to complete a new value of $x_3$. All processes are repeated by returning to the first equation until the solutions converge closely enough to the true values.

Convergence can be checked by using

$$\left| \frac{x_i^j - x_i^{j-1}}{x_i^j} \right| 100\% < \varepsilon_s \tag{B.5}$$

for all $i$, where $j$ and $j-1$ are the present and previous iterations and $\varepsilon_s$ the precision error.

A psudocode for the Gauss-Seidel follows;

Input $n$, $a_{ij}$, $b_i$, $x_i$, $M$, $\varepsilon_s$

for $k = 1$ to $M$ do

for $i = 1$ to $n$ do

$$x_i \longleftarrow \left( b_i - \sum_{\substack{i=1 \\ j \neq i}}^{n} a_{ij} x_j \right) / a_{ii}$$

end do

if $\left| \frac{x_i^j - x_i^{j-1}}{x_i^j} \right| 100\% < \varepsilon_s$ end do

output $x_i$

end do

The Gauss-Seidel method can be modified by using relaxation to enhance convergence. After each new value of $x$ is computed, that value is modified by a weighted average of the previous and the present values

$$x_i^{new} = \lambda x_i^{new} + (1-\lambda)\, x_i^{old}, \tag{B.6}$$

where $\lambda$ is a weighting factor which is value between 0 and 2.

If $\lambda$ is a value between 0 and 1, the type of modification is called under relaxation. It is used to make a non-convergent system converge or to fasten convergence by slowing down oscillations.

If the new value is moving in the correct direction toward the true solution but at too slow rate. Values of $\lambda$ between 1 and 2 is used to accelerate the convergence of a system. This type of modification is called successive or simultaneous over relaxation (SOR).

# VITAE

Mr. Charnwit Ruangchalermwong was born on April 4th, 1978 at Songkhla. He received a B.Sc. degree (first class honor) in physics from Prince of Songkhla University, Songkhla, Thailand in 2000.

## Conference Presentations:

2004 C. Ruangchalermwong, S. Chatraphorn and K. Yoodee. Optimization of front-contact grids for small-size solar cells. The 4th National Symposium on Graduate Research, Chiangmai University (August 10-11, 2004): O-ST-137

2004 C. Ruangchalermwong, S. Chatraphorn and K. Yoodee. A Numerical Method to optimize front-contact grids for small-size solar cells. 30th Congress on Science and Technology of Thailand, Srinakarinwirot University (October 19-21, 2004): D00422004

2005 C. Ruangchalermwong, S. Chatraphorn, C. Chityuttakan and K. Yoodee. Optimal Design of Collector Grid for CIGS Thin Film Solar Cells. 9th Annual National Symposium on Computational Science and Engineering, Mahidol University (March 23-25, 2005): CP1